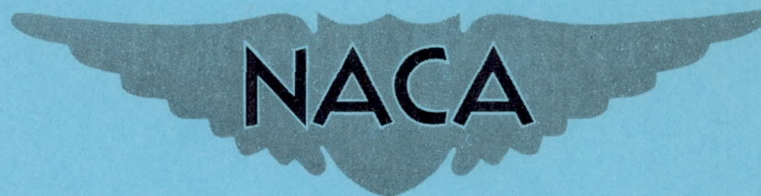


NACA RM No. L7J15



# RESEARCH MEMORANDUM

SUPERSONIC-TUNNEL TESTS OF TWO SUPERSONIC  
AIRPLANE MODEL CONFIGURATIONS

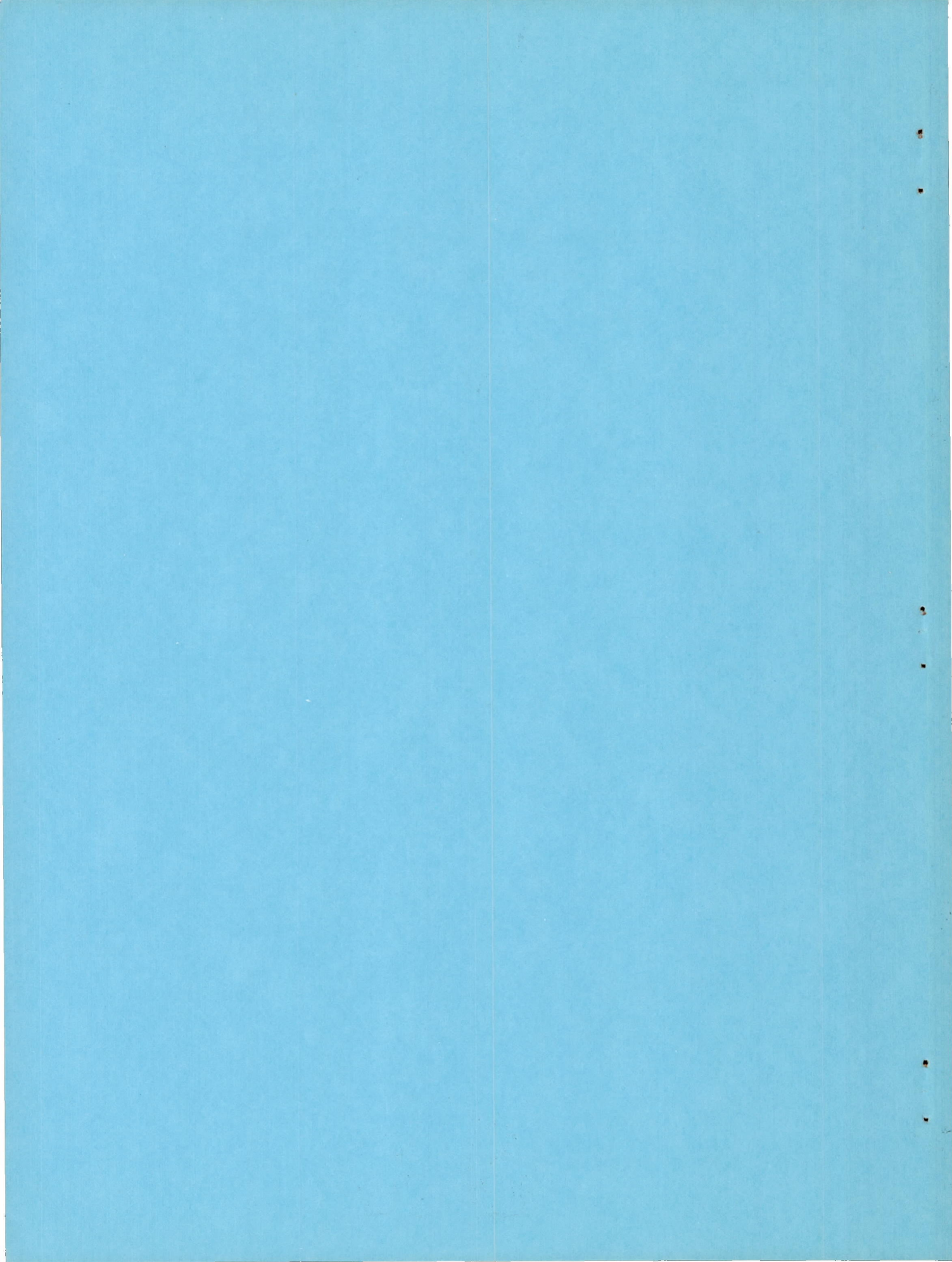
By

Macon C. Ellis, Jr., Lowell E. Hasel,  
and Carl E. Grigsby

Langley Memorial Aeronautical Laboratory  
Langley Field, Va.

NATIONAL ADVISORY COMMITTEE  
FOR AERONAUTICS  
WASHINGTON

December 31, 1947  
Declassified June 24, 1958



## NATIONAL ADVISORY COMMITTEE FOR AERONAUTICS

## RESEARCH MEMORANDUM

SUPERSONIC-TUNNEL TESTS OF TWO SUPERSONIC  
AIRPLANE MODEL CONFIGURATIONSBy Macon C. Ellis, Jr., Lowell E. Hasel,  
and Carl E. Grigsby

## SUMMARY

Supersonic-tunnel tests of two models of similar supersonic airplane configurations were made at Mach numbers of 1.55, 1.90, and 2.32 to determine values of the drag, lift, pitching moment, yawing moment, and side force. The two models had bodies, wings, and horizontal tails of similar geometry, the horizontal lifting surfaces having taper ratios of 2, aspect ratios of about 4, and leading-edge sweepback angles of about  $43^\circ$ . The principal difference between the models was the vertical wing location relative to the body axis and horizontal tail - one model had a high wing and one model had a low wing. The test results indicated no difference in the lift characteristics of the two models and small differences in the drag characteristics. The most significant results shown by the tests were the variation with Mach number of the differences between pitching-moment values for the two models, indicating the probability of differences in the rates of change of downwash angle with angle of attack for the two horizontal-tail locations relative to the wing.

## INTRODUCTION

The increased attention to supersonic aircraft and missile design over the past few years has greatly accelerated the need for basic supersonic aerodynamic information. Theoretical work has increasingly provided methods for calculating the basic aerodynamic characteristics of components such as bodies and a variety of wing plan forms; however, very little experimental data is available to check the theory or to predict the effect on lifting surfaces of a disturbed stream such as that produced by a supersonic airplane fuselage or by another lifting surface. Theoretical methods at present appear very awkward for calculating the characteristics of complete supersonic airplane configurations; thus, tests are, at the present time, the only adequate means for studying such cases. Because of the general interest in the information it might provide, tests of two supersonic airplane model configurations were made in the Langley 9-inch supersonic tunnel.

The configurations tested do not represent designs approximating optimums from present-day considerations, since their basic lines were conceived in the early part of 1946. The models represent two versions of a supersonic research airplane which was intended to be carried to high altitude by a "mother" ship, released, and accelerated to supersonic speeds by rocket motors of moderate duration. The two models had similar bodies and  $43^\circ$  sweptback wings and tail surfaces, the wings having sharp-edged circular-arc sections. The primary difference in the two models was the vertical location of the wing - one model had the wing located in a high position on the body, whereas the other model had the wing located in a low position on the body. Tests of both models at Mach numbers of 1.55, 1.90, and 2.32 were made to determine the values of lift, drag, pitching moment, yawing moment, and side force through angles of pitch and yaw. The tests were restricted to fairly low angle ranges around zero lift because of load limitations on the force-measuring equipment. Data from these tests are presented herein.

#### SYMBOLS

M	Mach number
$\rho$	stream density
q	dynamic pressure $\left(\frac{1}{2}\rho V^2\right)$
b	maximum wing span
c	moment reference chord (See table I.)
R	Reynolds number referred to c
S	wing area (See table I.)
$C_L$	lift coefficient (Lift/qS)
$C_D$	drag coefficient (Drag/qS)
$C_m$	pitching-moment coefficient (Pitching moment/qSc)
$C_n$	yawing-moment coefficient (Yawing moment/qSb)
$C_Y$	side-force coefficient (referred to wind axis) (Side force/qS)
$\alpha$	angle of attack
$\psi$	angle of yaw

## APPARATUS AND TEST METHODS

## Wind Tunnel and Model Support

The Langley 9-inch supersonic tunnel in which the present tests were made is a closed-return type which makes possible control of the humidity and pressure of the enclosed air. During the present tests, the quantity of water vapor present in the tunnel air was kept to values sufficiently low so that the effects of condensation in the supersonic nozzle were negligible. Changes in test Mach number were provided by interchangeable nozzle blocks forming test sections approximately 9 inches square. For qualitative, visual-flow observations, a schlieren optical system is provided. Eleven fine-mesh turbulence-damping screens are provided in the settling chamber ahead of the nozzles.

The models were mounted from the rear on sting supports which connected to the scales through the sting windshield with small clearance as shown in figure 1. The scales measure three components in a horizontal plane only; thus, for yaw results, the models were rotated 90°. For yaw results at different pitch angles, interchangeable bent sections of sting as shown in figure 1 were inserted just aft the rear of the model. For integrating the pressure forces acting on the sting, fixed orifices in the sting were provided upstream and downstream of the windshield "slot." Owing to the fact that the sting between the windshield slot and the rear of the model included a removable section, the extent of the fixed orifices upstream was limited to a station aft the removable section rear joint.

## Description of Models

Dimensions of the supersonic airplane models tested are shown in figures 2 and 3. Because of the difficulty of accurately measuring the models, dimensions are shown to only  $\pm 0.01$  inch. Actually, the model components were constructed to much smaller tolerances. Considerable care was taken to make all surfaces smooth and free from scratches and to make the leading and trailing edges of the wings as sharp as possible. Model 2 shown in figure 3 is the later version and it is seen that the main differences from model 1 are the lower wing location on the fuselage and the larger vertical tail. These changes were indicated by directional stability results from low-speed wind-tunnel model tests. Another difference between the models that should be noted is the longer tail arm for model 2. Photographs of the two models shown in figure 4 are included to show the filleting and fairing details between the model components.

### Test Methods

The diameter of the sting support for both models is the same as that of the rocket-discharge station at the rear of the fuselage. This scheme obviously suggests itself since the sting can be assumed to occupy the same volume as the initial part of the rocket-jet exhausting at stream pressure. Furthermore, if there are no interacting effects between the flow over the sting and the flow over the rear part of the body, the drag of the model can be measured and clearly separated from any thrust considerations. The significant departures from these assumptions for the test setup are, first, that the actual rocket-jet would probably be discharging at pressures above or below stream pressure most of the time and affecting the flow over the rear of the body, and, second, that the effects felt forward through subsonic portions of the jet and stream mixing region on the flow over the rear part of the body will be different from the effects felt forward through the sting boundary layer. Because of the foregoing considerations, it was felt at the start that the best approach to the assumed simulated conditions was to maintain the boundary layer over the sting as thin as possible in order to minimize the effects of disturbances in the region of the windshield slot on the flow over the rear part of the body. Consequently, the pressure in the sting-shield-and-balance-enclosing box was kept as low as possible so that a suction into the box always existed at the windshield slot. Efforts to obtain consistent data, especially moment data, with this setup proved futile until pressure-distribution measurements around the sting revealed significant pressure forces on the sting in the region of the slot. It thus became necessary to install sufficient orifices on the sting to integrate the pressure distribution around and along the sting and obtain these tare forces. The orifices extended along the sting only a sufficient distance to measure the forces in the region of the slot (about two sting diameters inside the windshield and one sting diameter outside). These orifices and connecting tubing were so arranged that force and pressure measurements could be made simultaneously. This arrangement was indicated after it was found that a set of pressure measurements could not be repeated in check tests owing to the fact that small, uncontrollable, and different eccentricities of the sting in the windshield altered the distribution of pressures around the spindle. It thus became necessary to integrate the pressure forces on the sting for each test point at each angle of attack of a model.

The forward extent of the fixed orifices was limited by the threaded joint in the sting. As was mentioned previously, a bent section of sting was inserted between this joint and the rear of the model to provide yaw angles when the models were pitched and pitch angles when the models were yawed. Because of forces acting on the bent sting section, pressure measurements for some of the tests were made on the bent section by means of orifices which had connecting tubes leading out of the sting into the

air stream in such a manner that it was unlikely that the connecting tubes would influence the pressure reading. Since the connecting tubes were ahead of the slot, they did influence the flow in the region of the slot; thus the assumption had to be made that the pressures forward on the sting were not influenced by the different flow conditions in the region of the slot. Measurement of the pressure forces on the forward part of the sting was found to yield significant corrections only for the yawing-moment measurements. In general, all of the sting pressure-force corrections had only small effect on the lift and side force. The significant effect of the sting pressure-force corrections on the moment is due mainly to the relatively large distance of the small forces from the moment-reference point in the region of the airplane center of gravity. All of the data in the present report have been corrected for only the pressure forces in the region of the slot; discussion of the effects of the pressure-force corrections for the remainder of the sting are included in the discussion of yawing-moment results. It should be mentioned that in all of the data the incremental angles of attack due to load deflections of the sting have been included.

## TEST RESULTS

### Precision of Data

The total forces on the models and support system were measured by means of self-balancing beam scales, the accuracy and reliability of which were very good for measuring the steady forces on the models in the tests. The maximum probable uncertainty of the coefficients due to scale errors is listed in the following table:

Coefficient \ M	2.33	1.90	1.55
$C_Y$	$\pm 0.0002$	$\pm 0.0002$	$\pm 0.0002$
$C_L$	.0002	.0002	.0002
$C_D$	.0002	.0002	.0002
$C_m$	.0013	.0013	.0011
$C_n$	.0004	.0004	.0003

Observation of the data will show that these errors are insignificant.

The total uncertainties of the coefficients involving corrections due to the sting pressure forces in the lift direction (all but  $C_D$ ) are not known due to the prohibitively tedious process of making sufficient pressure measurements for precise evaluation. The precision of the drag measurements was better than that of lift and moment measurements because the sting side forces had no effect on the drag at zero angle of attack and little effect at the small angles for the tests. The effects of viscous drag forces due to the flow over the sting in the region of the slot were found from auxiliary tests to be small. The total force indicated on the drag scale consisted of the drag of the model plus a pressure force equal to the ~~sting and balance enclosing box~~ pressure minus stream pressure multiplied by the sting cross-section area. In the tests, this pressure force on the sting in the axial direction was from 2 to 5 percent of the total force and could be evaluated within about  $\pm 10$  percent. For the typical value of  $C_D = 0.050$ , the accumulated uncertainty in the drag measurement is then about  $\pm 1$  percent.

Whereas the absolute angles of attack of the models relative to the stream direction are in doubt in some cases up to  $\pm 0.3^\circ$ , the angles of attack relative to each other in a run are uncertain only to a maximum of  $\pm 0.03^\circ$ . The errors up to  $\pm 0.3^\circ$  arose from the method used to pitch or yaw the model in a vertical plane while varying the angle of attack in a horizontal plane.

The maximum variation of Mach number and static pressure obtained from stream surveys made in the model test region of each of the three nozzles is shown in the following table:

$M_{\text{average}}$	$M_{\text{variation}}$	Maximum variation of static pressure (percent)
1.55	1.54 - 1.56	$\pm 1.3$
1.90	1.89 - 1.91	$\pm 1.5$
2.32	2.31 - 2.33	$\pm 1.5$

The maximum error in the data due to these small variations of Mach number and static pressure is not known; however, it is believed that other errors such as those already discussed are of greater significance.



## Reynolds Numbers of Tests

The test values of Reynolds number referred to the same chord as the moment values (approximately the mean wing chord) are given in the following table:

M	$R \times 10^{-6}$
1.55	0.41
1.90	.37
2.32	.31

Results at  $M = 1.90$ 

Results at  $M = 1.90$  are presented first because the first tests establishing procedures were made at this Mach number and the bulk of data is largest. The results showing the variation of  $C_m$ ,  $C_L$ , and  $C_D$  with angle of attack for models 1 and 2 at various yaw angles are given in figures 5 and 6. A typical set of data uncorrected for sting side forces is shown in figure 5(a). The results showing the variation of  $C_n$ ,  $C_Y$ , and  $C_D$  with angle of yaw for models 1 and 2 at various pitch angles are given in figures 7 and 8. Unless otherwise specified, the results for model 2 are for the model with the ventral fin. Shown in figure 9 are yaw results for model 2 with the ventral fin off.

The pitching moment and lift-curve slopes and angles of zero lift are collected from figures 5 and 6 and shown as a function of yaw angle for the two models in figure 10. It is seen that the tests show no significant variation with yaw angle. The scatter of zero-lift angles is due to the method of varying the yaw angle. The tunnel angle-of-attack changing mechanism varies the model angle in only one plane. Angles from this plane were obtained with removable sting sections inserted just aft the rear of the model. Although the angles of the sting sections were precise, the shims necessary to establish the correct roll position of the models introduced angle errors which shifted the model at the various yaw angles randomly away from the zero angle reference (stream direction). The pitching-moment variation with lift for model 1 shown in figure 11 supports this assertion by showing random scatter about a single line for most of the test points. Similar results given for model 2 in figure 12 show even less scatter.

The lift-curve-slope values shown in figure 10 are seen to be the same for both models. Reference to table I shows the total horizontal lifting-surface area to be very close to the same for both models; thus the lift is indicated to be unaffected by the differences in geometry

between the two models. The pitching-moment-curve slope  $\frac{dC_m}{d\alpha}$  results

show higher negative values for model 2. Comparison between the pitching-moment values for the two models is complicated by the longer tail arm and larger tail area for model 2 and the fact that the incremental lifts of the tails were not measured. Furthermore, the moment reference points for the two models are not at the same point relative to the approximately similar wing-plan geometries. In order to obtain moment-curve-slope values for model 2 referenced to the same point relative to the wing vertex as model 1 values, the model 2 values should be increased by 0.0012. Increasing model 2 values thus, it is seen that model 2 has an average value of moment-curve slope about 0.0037 greater than model 1. If it is assumed that the lift-curve slopes of the wing and tail are the same and that the center of lift of each component acts at its center of area, then the moment-curve-slope increase indicated for model 2 with the longer tail arm and larger tail area is only about 0.0010. If the wing lift is assumed to act farther forward at the moment reference point, the moment-curve-slope increase indicated for model 2 is still only about 0.0019. The large difference between these estimates and the measured pitching-moment increase indicates the possibility of differences in the rates of change of downwash angle with angle of attack at the two vertical locations of the horizontal tail relative to the wing.

The yawing-moment and side-force curve slopes and angles of zero side force are collected from figures 7 and 8 and shown as a function of angle of attack for the two models in figure 13. It is seen that the tests show no significant variation with angle of attack for the small angles around zero lift. The larger scatter of the yawing-moment and side-force data as compared with the pitching-moment and lift data is mainly due to the fact that the sting pressure-force corrections represented a larger fraction of the measured quantities. The data show higher values of both yawing moment and side force as would be expected for model 2 with the larger vertical tail and longer tail arm. It appears that in all cases increasing the vertical-tail area produces increases in the yawing moment greater than the proportional area increases, whereas the side-force increases are either about equivalent to or less than the proportional area increases. Discussion of the relative increases of yawing moment and side force is probably complicated by the effect of the wing and tail on the flow over the rear of the body, changes in which probably lead to significant changes in the body moment and the moment due to sidewash at the tail. Scatter of the angles of zero side force are due in part to the angle errors introduced as previously mentioned by the bent sting sections. The angle for zero side force and yawing moment should of course be zero since the model is symmetrical about the xz-plane. It is seen that in figure 14 for model 1 there are systematic sets of points for the various pitch angles that would give curves of the variation of yawing moment with side force which would not go through the origin. The reason for this discrepancy is not fully understood; however, the mean curve for all the data does go through the origin, indicating the model

to have a plane of symmetry. The results for model 2 given in figure 14 show a mean curve that does not go through the origin, indicating model 2 to have no plane of symmetry. Measurements of model 2 vertical-tail angle setting indicated that it might be offset by as much as  $1^\circ$  from the xz-plane.

The drag results shown in figure 15 indicate slightly lower drags for model 2. Removing the ventral fin from model 2 is indicated to decrease the drag by about 4 percent.

#### Results at $M = 2.32$

The results showing the variation of  $C_M$ ,  $C_L$ , and  $C_D$  with angle of attack for both models are given in figures 16 and 17. The number of yaw angles at which tests were made was restricted because the  $M = 1.90$  results showed no significant effects. Yawing-moment and side-force results are given in figure 18 for only model 2 at one pitch angle.

#### Results at $M = 1.55$

The results showing the variation of  $C_M$ ,  $C_L$ , and  $C_D$  with angle of attack for models 1 and 2 are given in figures 19 and 20. The repeat runs of figure 20 were made to check various schemes for integrating the pressure forces forward on the sting with only a limited number of pressure readings. Although the effects on the moment of approximately accounting for the pressures forces on the forward part of the sting were small, there remains an unexplainable spread from the maximum indicated pitching-moment-curve-slope value to the minimum indicated value of about 13 percent. Yaw results for models 1 and 2 are shown in figures 21 and 22.

#### Summary of Test Results

The pitching-moment and lift results are collected from the data and shown in figure 23 as a function of Mach number. It is seen that the lift-curve slopes are the same for both models through the test Mach number range. For comparison with the lift results, the theoretical values of lift-curve slope from the linearized theory are shown for the two-dimensional or infinite aspect ratio case and for a wing with the same plan form as the model wing. Comparison of the theoretical lift-curve-slope values with the test values based on the total wing and horizontal-tail area indicates a convergence of the lift-curve-slope variation with Mach number as the Mach number increases. This convergence

trend between the theory and tests has also been observed in other tests of swept wings in this Mach number range in the Langley 9-inch supersonic tunnel.

The pitching-moment values shown in figure 23 show considerable scatter at each Mach number, thus the curves of  $dC_M/dC_L$  are shaded between the limits of scatter for each model. Even though the reasons for the scattered values are not completely understood, it seems reasonable to assert that the large differences in the character of the two shaded curves are indicative of different trends for the two models. It was stated in the discussion of the  $M = 1.90$  results that the differences in pitching-moment values at  $M = 1.90$  indicated the possibility of differences in the rates of change of downwash angle with angle of attack at the two vertical-tail locations relative to the wing. The test results indicate Mach number, as well as tail location, to be an important variable in longitudinal-stability considerations. Lack of knowledge of the downwash distribution in the wing wake precludes any detailed discussion of the differences in static longitudinal stability indicated by the tests.

The yawing-moment results shown in figure 24 indicate both models to be decreasing their margin of static directional stability as the Mach number increases. Considering the body and vertical tail only to be the controlling elements, this trend might be expected, since the moment due to the side force of the vertical tail probably decreases with increasing Mach number at a greater rate than the moment due to the body. For small yaw angles, it was estimated that the stabilizing effect of the spanwise shift of the wing drag component is very small.

The drag results shown in figures 24 and 25 show the drag of model 1 to be highest throughout the test Mach number range. Addition of the ventral fin to model 2 at  $M = 1.90$  is indicated to increase the drag by about one-half the incremental difference in drag between model 1 and model 2 without the ventral fin. The increased drag of model 1 above the drag of model 2 with the ventral fin is probably due to changes in interference among the model components. Perhaps the closer proximity of the boundary-layer wake of model 1 wing to the horizontal- and vertical-tail juncture and body and vertical-tail juncture has contributed to the increase.

### Schlieren Photographs

As a matter of general interest, some schlieren photographs of the flow about the models at  $M = 1.90$  are presented in figure 26. All of the photographs shown were taken with the schlieren knife-edge horizontal, thus show only vertical density gradients. It should be recognized in observing the photographs that the disturbances shown are generally the

limits of only that portion of three-dimensional wave patterns close to a vertical plane through the axis of the models. It should also be realized that the location and shape of waves enclosed unsymmetrically inside an outer conical or three-dimensional wave are distorted somewhat by the optical system. The disturbances shown in figure 26(a), for instance, progressing from the nose aft are the conical head wave (distorted by the wave from the canopy-fuselage juncture), waves from the wing leading-edge-fuselage juncture, waves from the wing trailing-edge-fuselage juncture, and waves from the tail surfaces. The horizontal-tail boundary-layer wake can be seen in figures 26(a) and (c) and the wing boundary-layer wake can be seen for model 2 in figure 26(c). The wing boundary-layer wake in figure 26(a) is located in the sting silhouette and cannot be seen. Apparent separation of the boundary layer from the body aft the wing is seen in figures 26(b), (c), and (d). This indicates that the adverse pressure gradients around the body presented by the shock waves at the wing leading- and trailing-edge junctures at the fuselage may be an important factor in considerations of the flow over the aft portion of bodies with wings.

Langley Memorial Aeronautical Laboratory  
National Advisory Committee for Aeronautics  
Langley Field, Va.

TABLE I. PERTINENT MODEL AREAS

[All areas given to model center line. All data coefficients based on wing area = 0.0337. Moment reference chord = 0.095 ft]

	Model 1	Model 2
Measured wing area, ft <sup>2</sup>	0.0337	0.0333
Measured horizontal tail area, ft <sup>2</sup>	.0054	.0057
Total of measured wing and horizontal tail areas, ft <sup>2</sup>	.0391	.0390
Measured vertical tail area, ft <sup>2</sup>	.0058	.0087
Measured ventral fin area, ft <sup>2</sup>	.0027	.0026
Total measured vertical fin area, ft <sup>2</sup>	.0085	.0113

NATIONAL ADVISORY  
COMMITTEE FOR AERONAUTICS

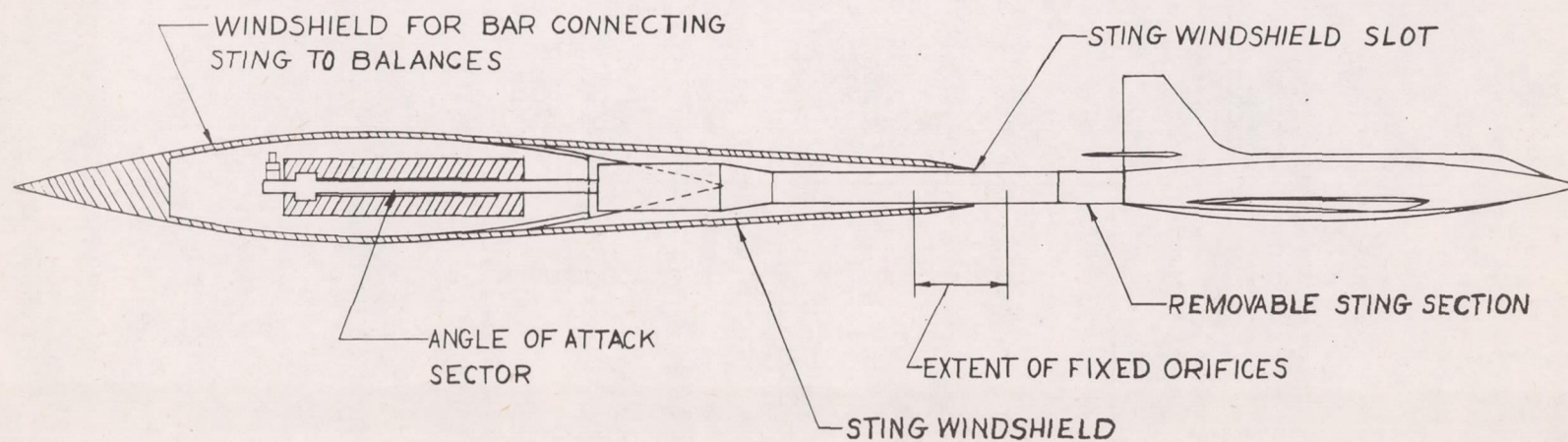
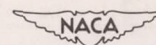


FIGURE 1.-MODEL AND STING SUPPORT SYSTEM.



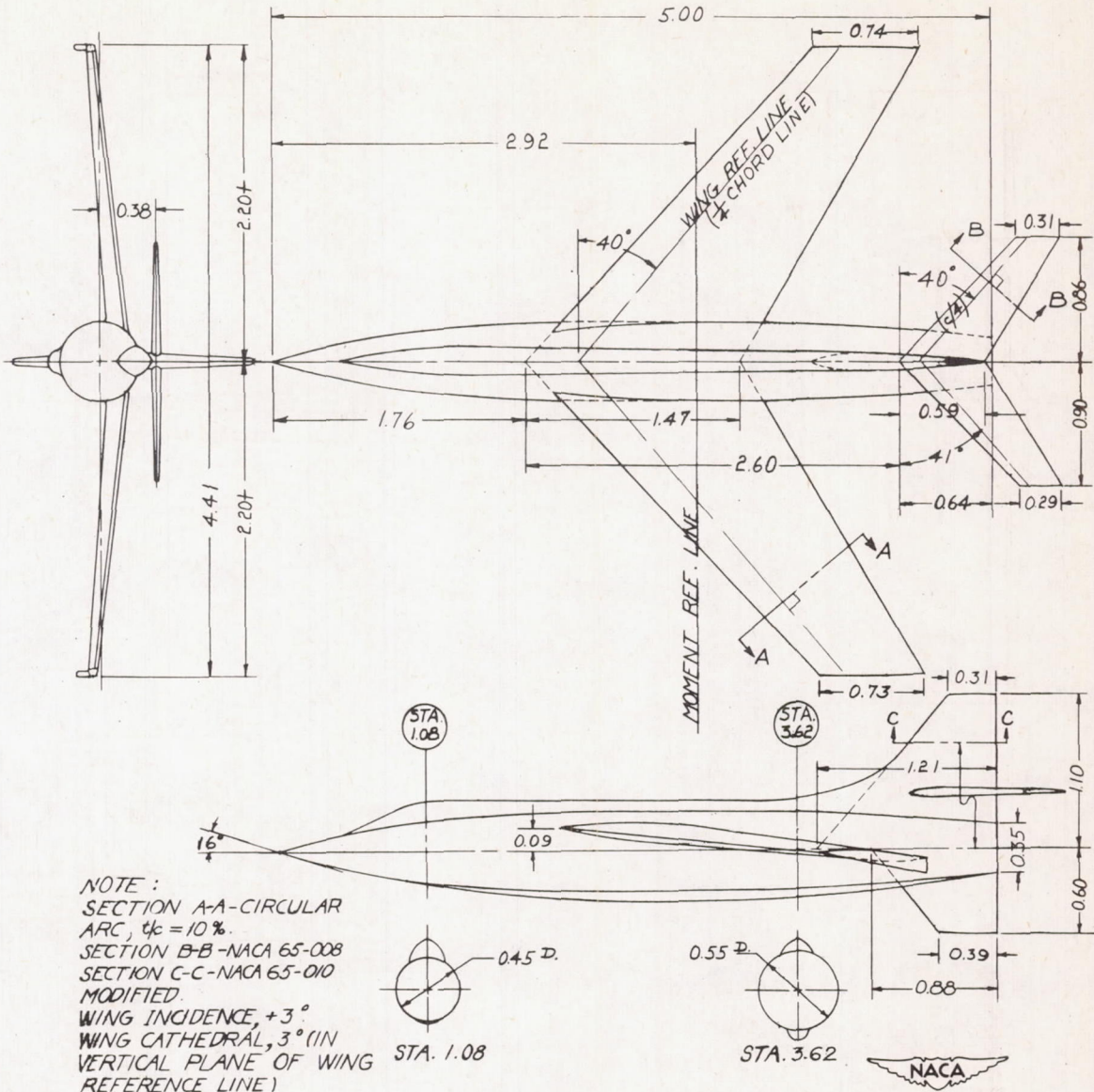


FIGURE 2-MODEL 1 DIMENSIONS (INCHES).



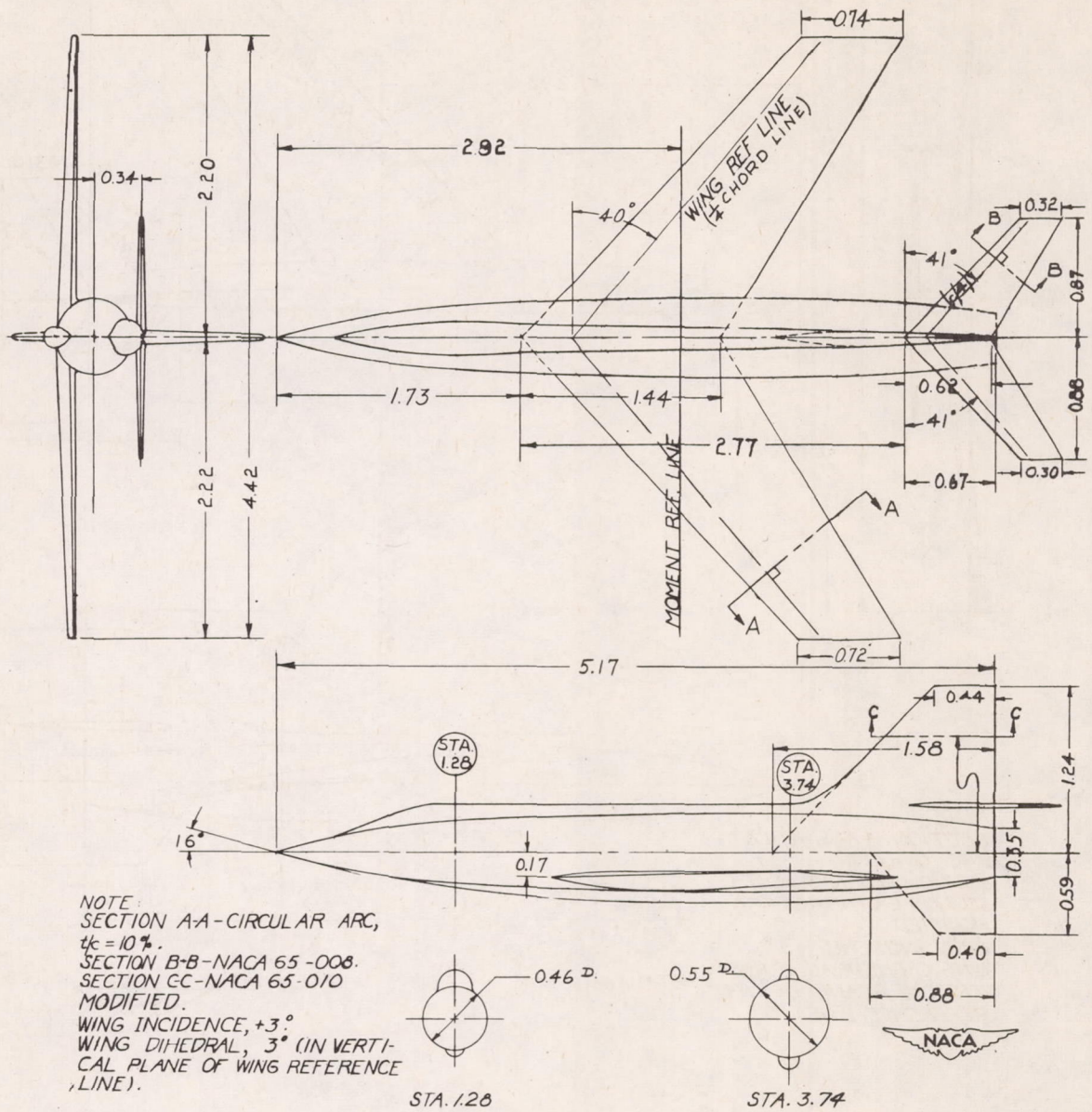
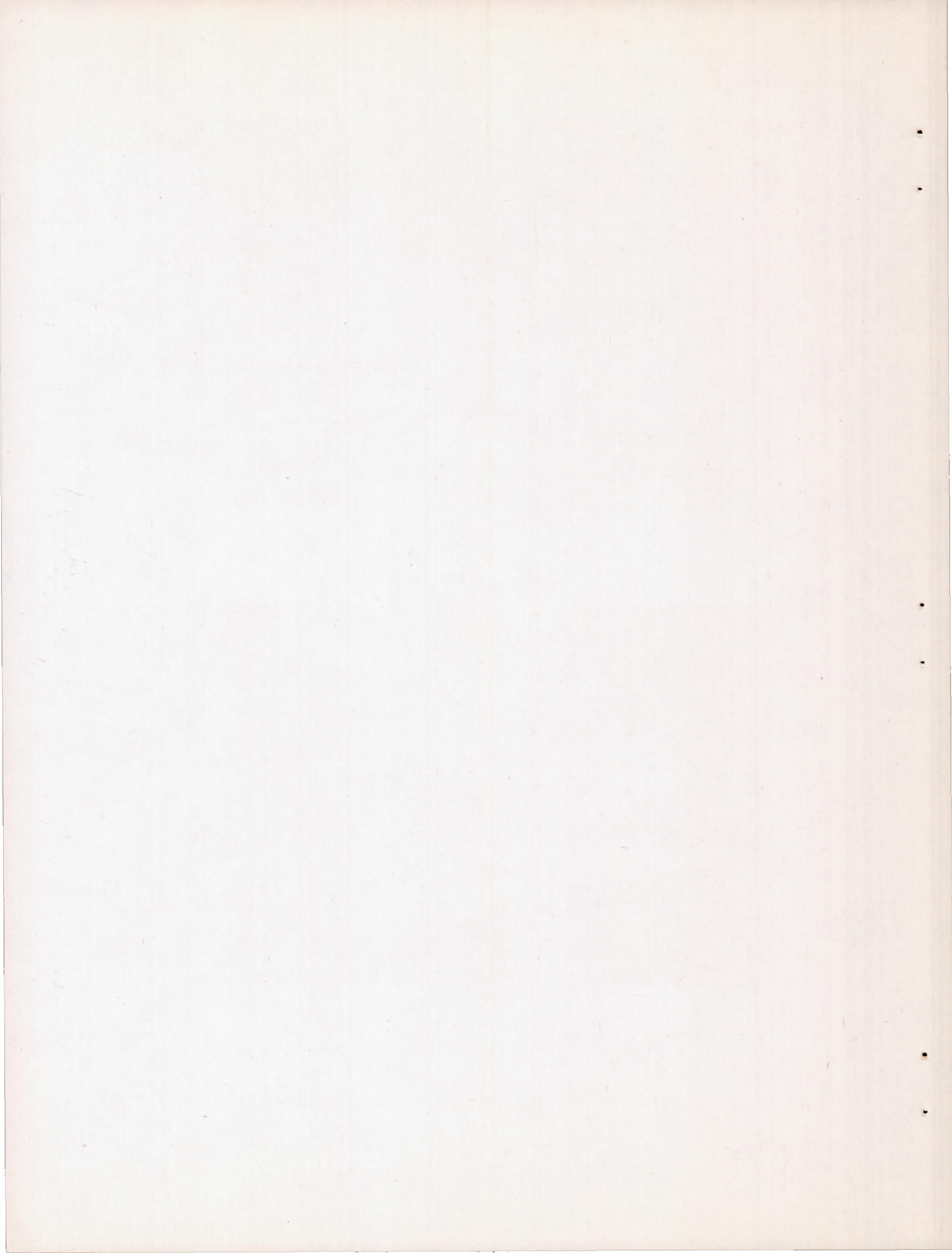
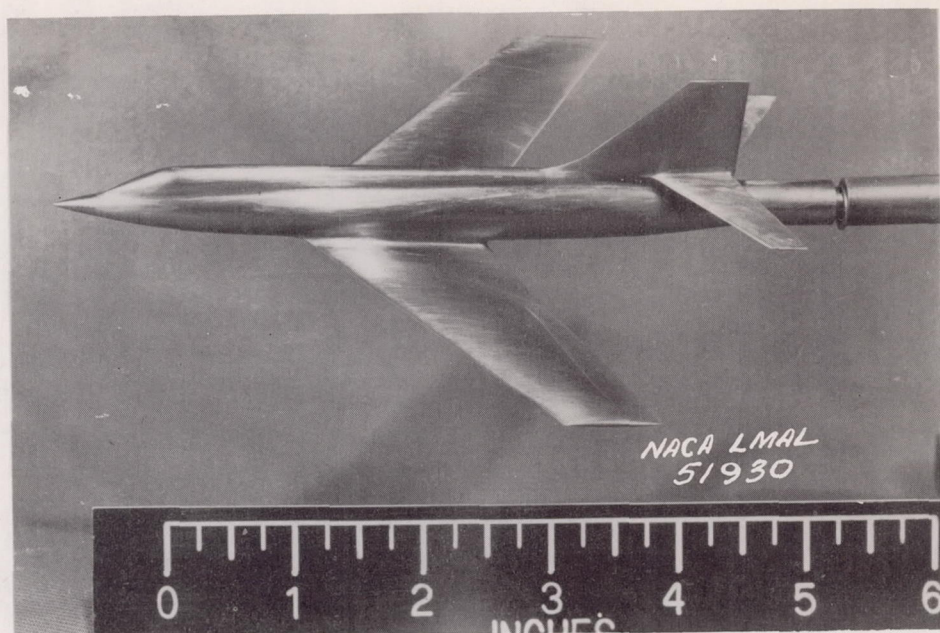
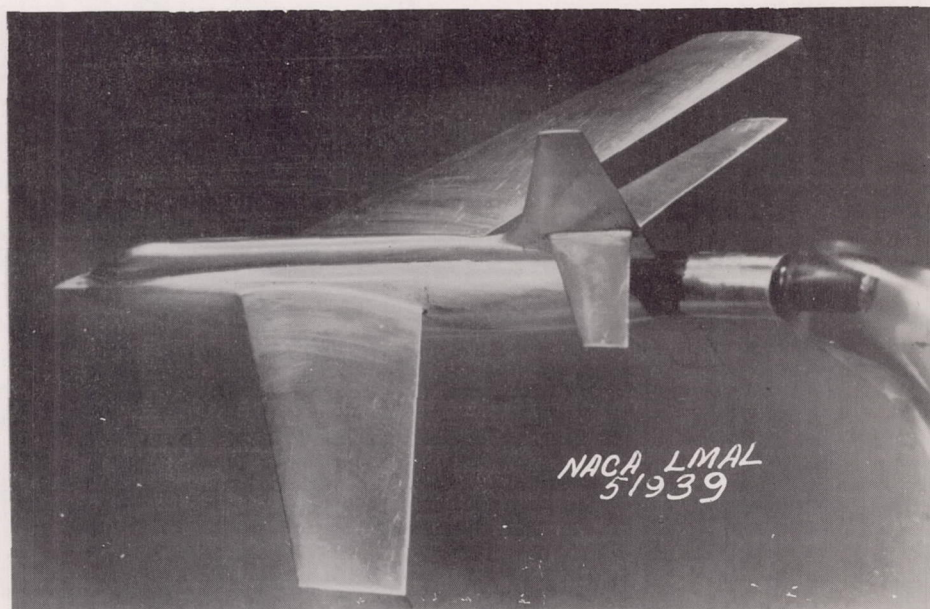


FIGURE 3. - MODEL 2 DIMENSIONS (INCHES).



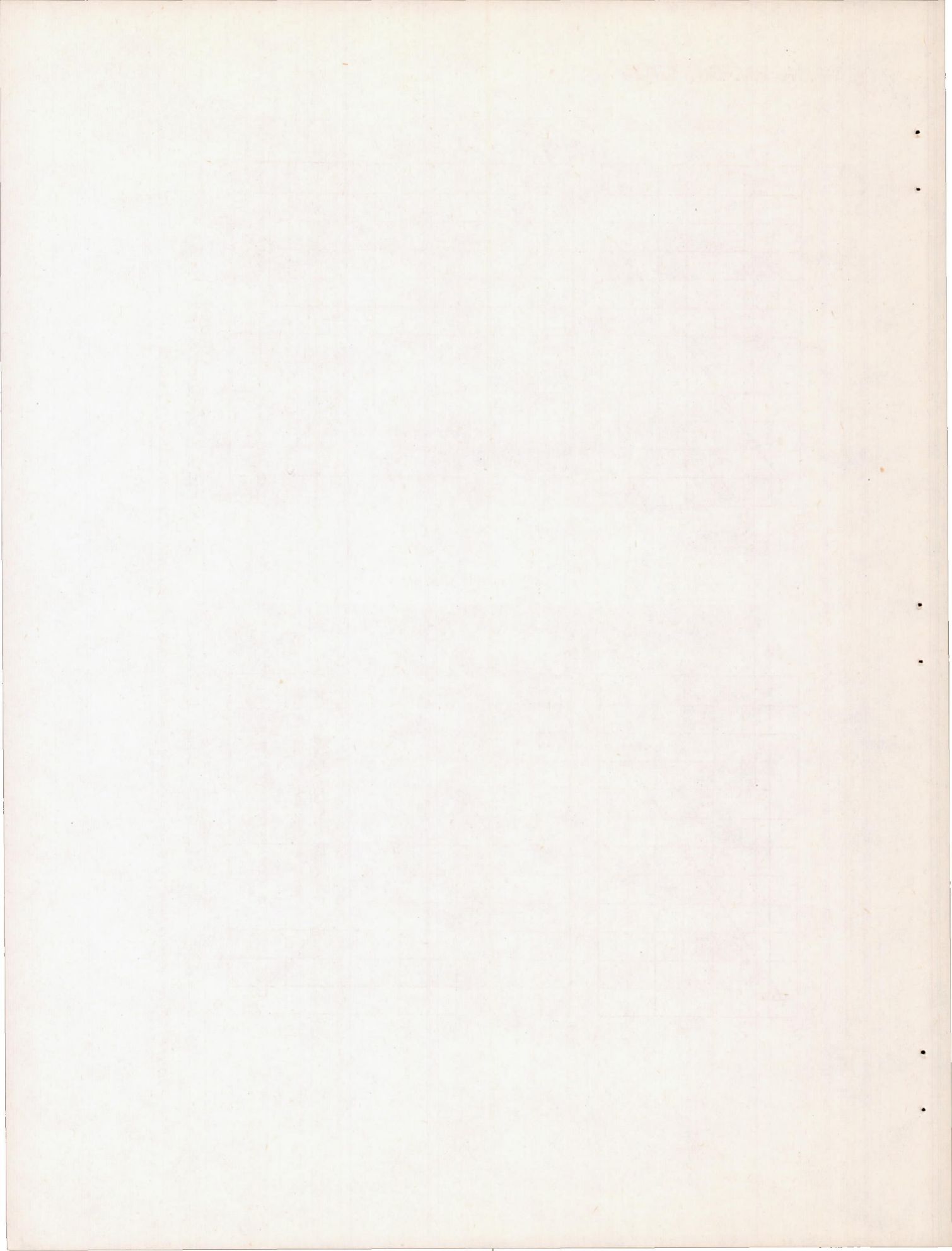


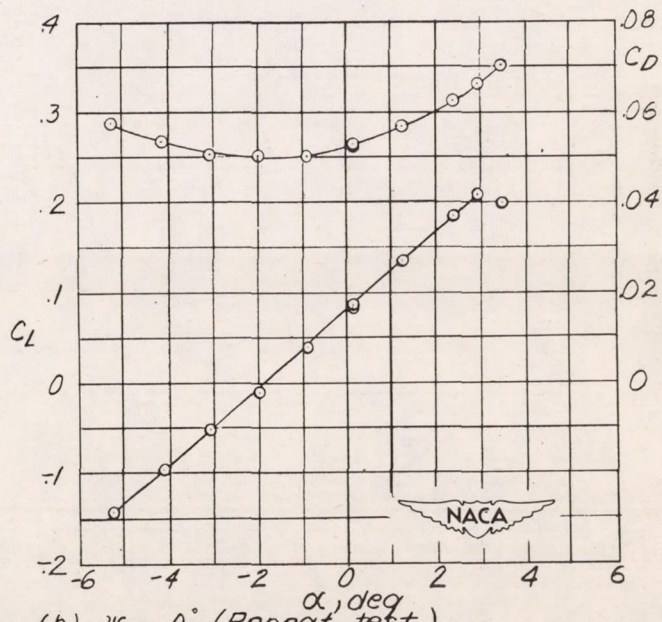
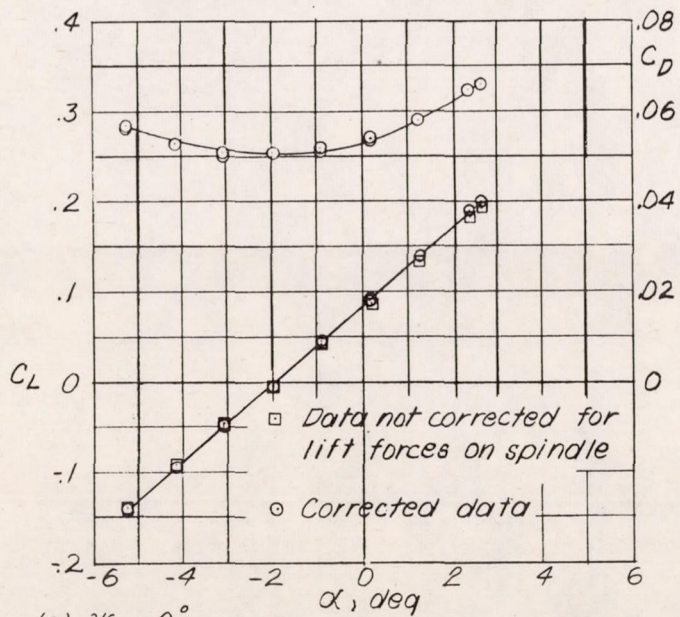
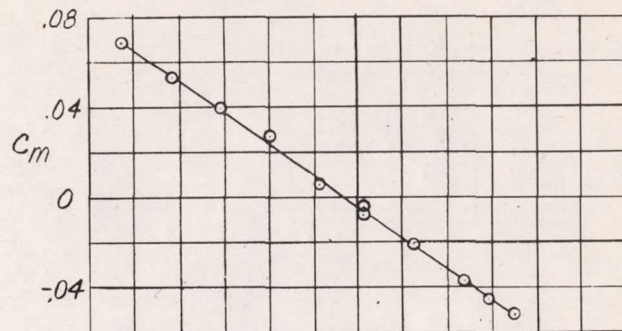
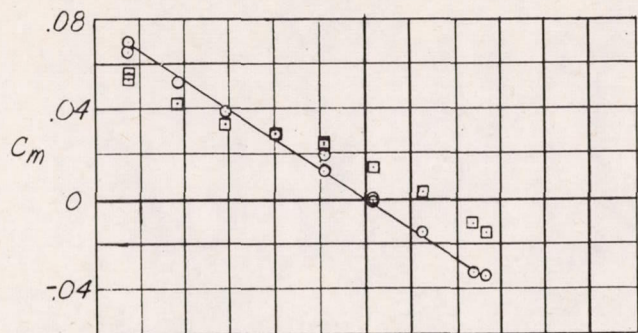
Model 2



Model 1

Figure 4.- Photographs of models 1 and 2.





(a)  $\psi = 0^\circ$

(b)  $\psi = 0^\circ$  (Repeat test).

Figure 5. - Variation of  $C_m$ ,  $C_L$  and  $C_D$  with angle of attack for model 1;  $M=1.90$ .

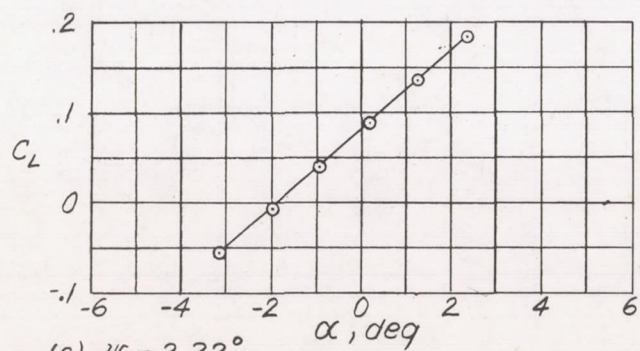
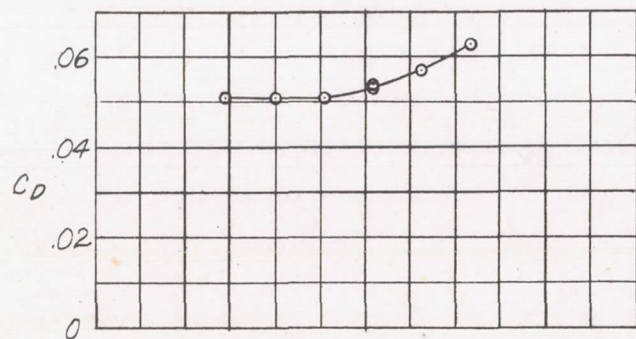
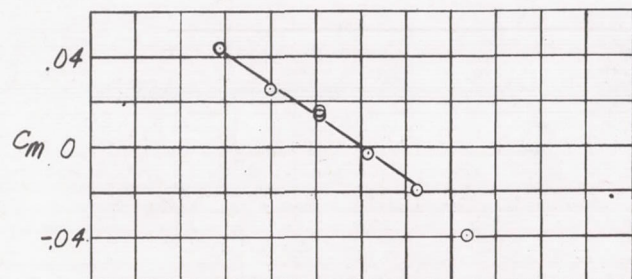
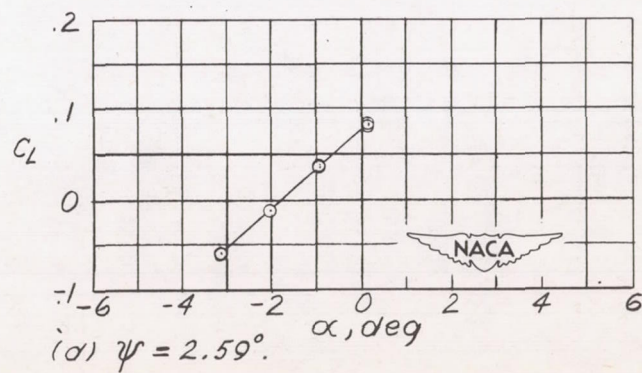
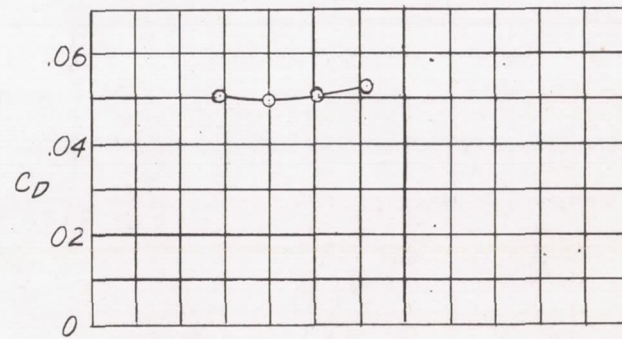
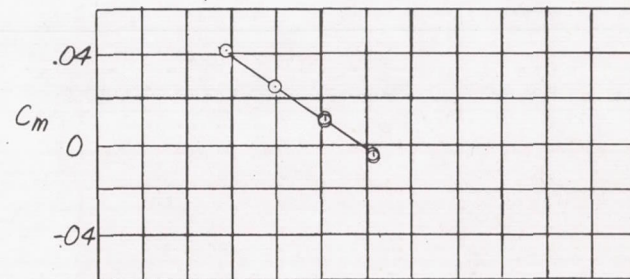
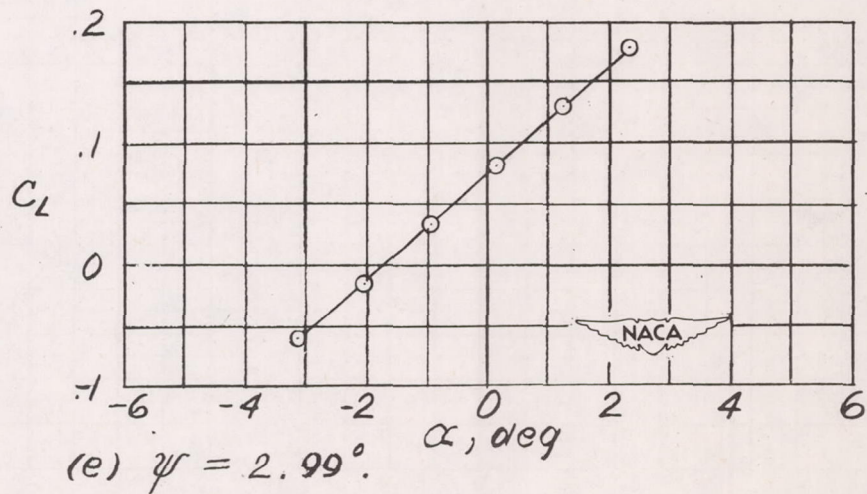
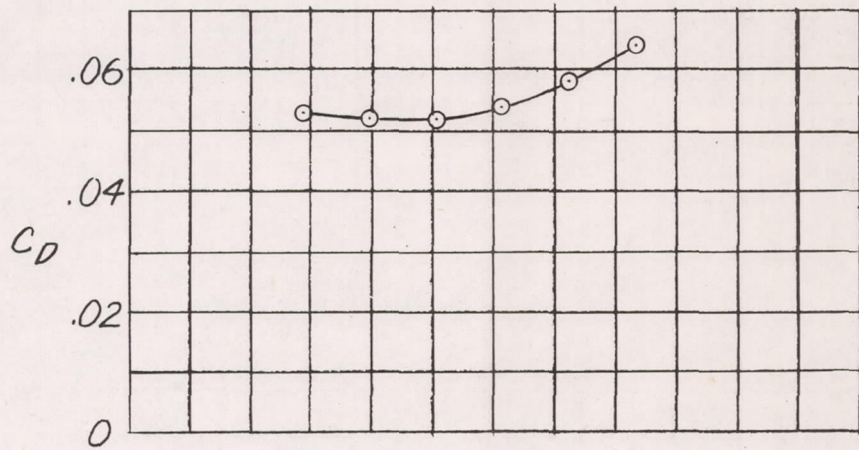
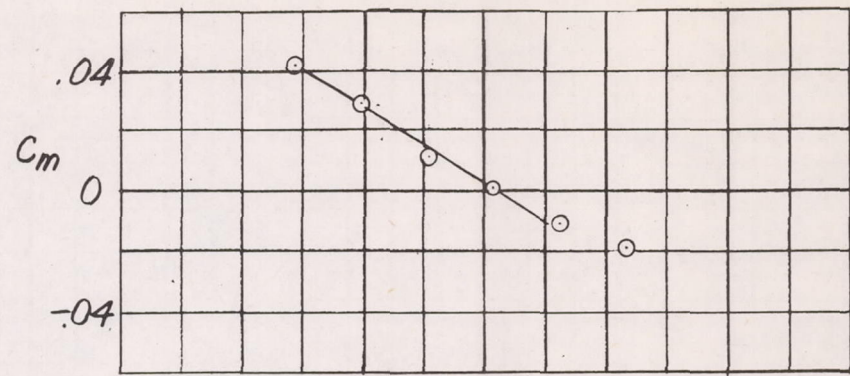
(c)  $\psi = 2.22^\circ$ .

Figure 5. — Continued.

(d)  $\psi = 2.59^\circ$ .



(e)  $\psi = 2.99^\circ$ .

Figure 5 . - Concluded.

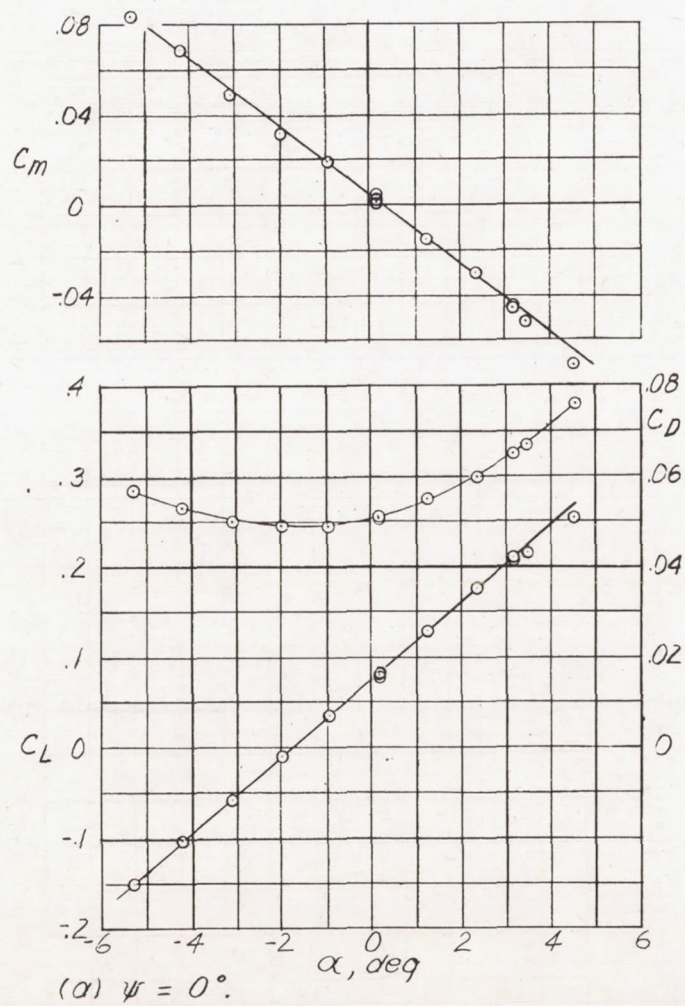


Figure 6. - Variation of  $C_m$ ,  $C_L$  and  $C_D$  with angle of attack for Model 2;  $M = 1.90$ .

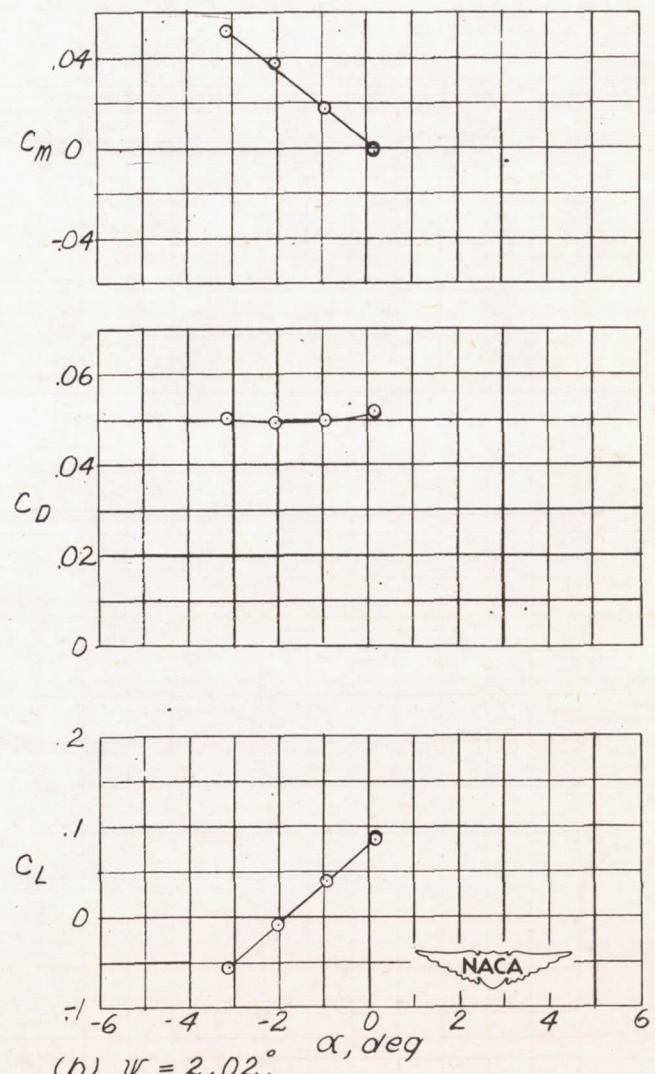
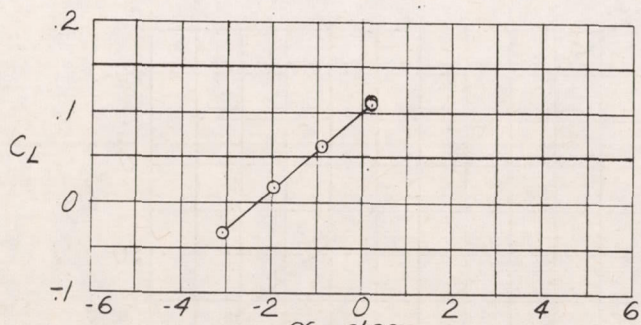
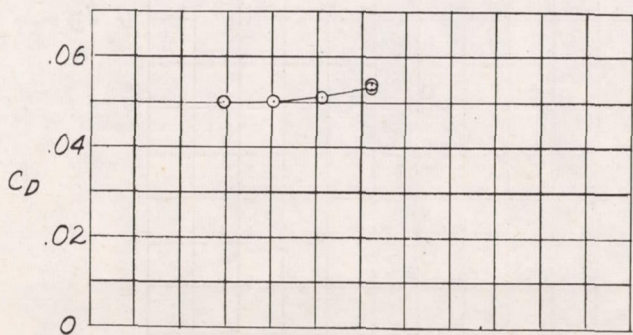
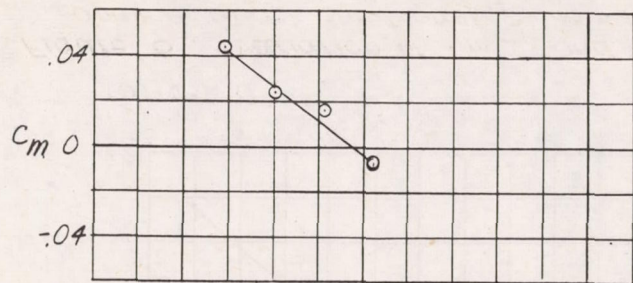


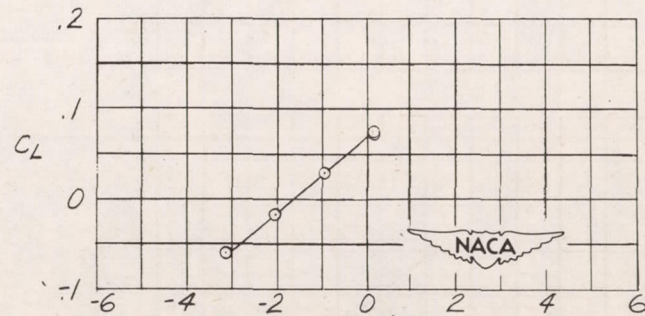
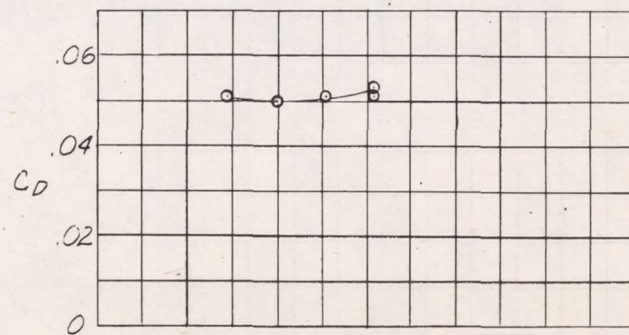
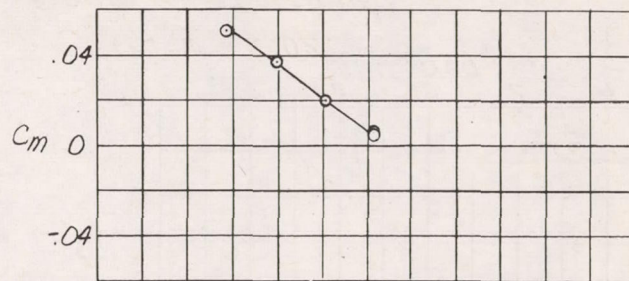
Figure 6. - Continued.





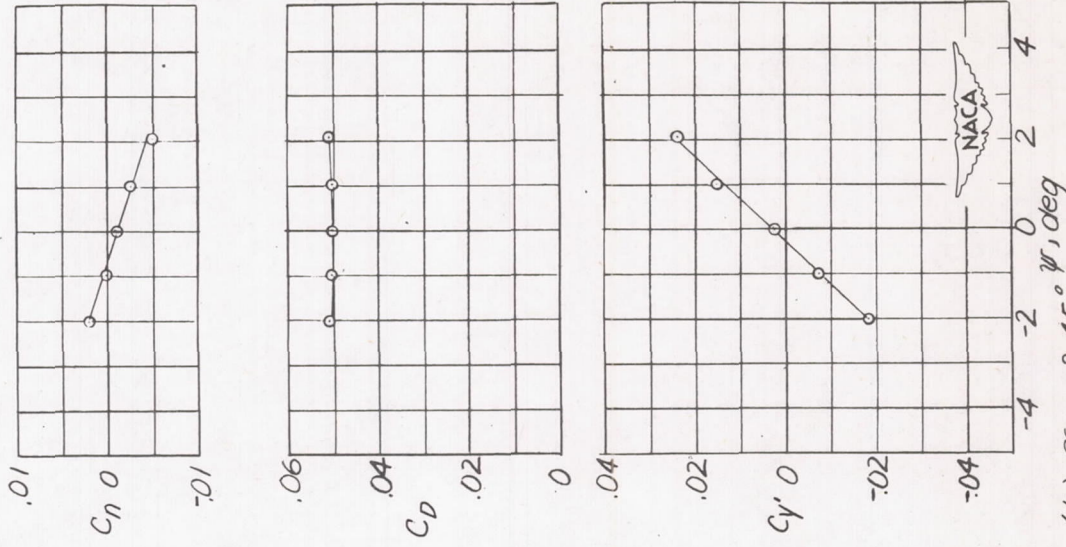
(c)  $\psi = 2.18^\circ$

Figure 6 . - Concluded.

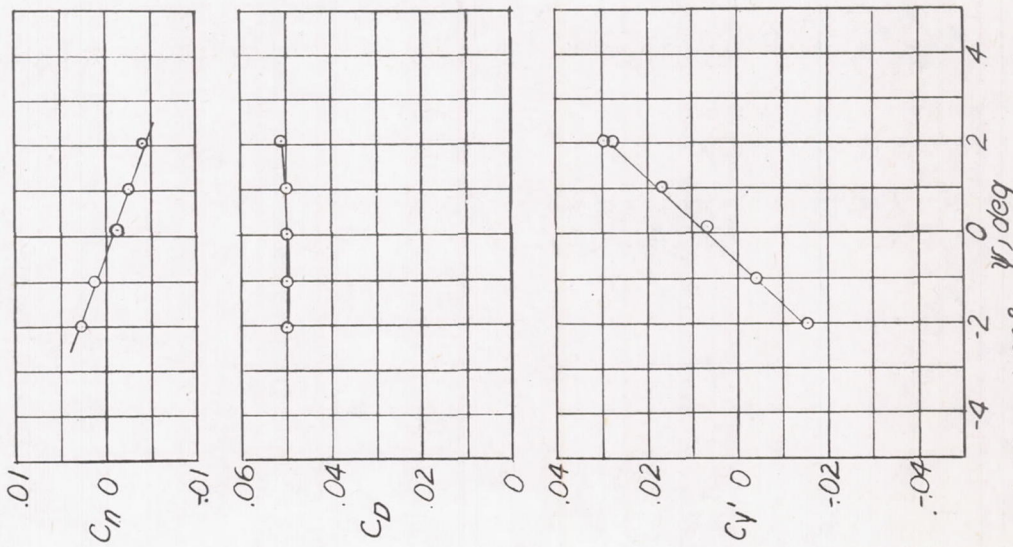


(d)  $\psi = 2.53^\circ$

Figure 6 . - Concluded.



(b)  $\alpha = -2.45^\circ$   $\psi$ , deg  
Figure 7. - Continued.



(a)  $\alpha = -1.60^\circ$   
Figure 7. - Variation of  $C_n$ ,  $C_{y'}$  and  $C_D$  with angle of yaw for Model 1;  $M = 1.90$ .

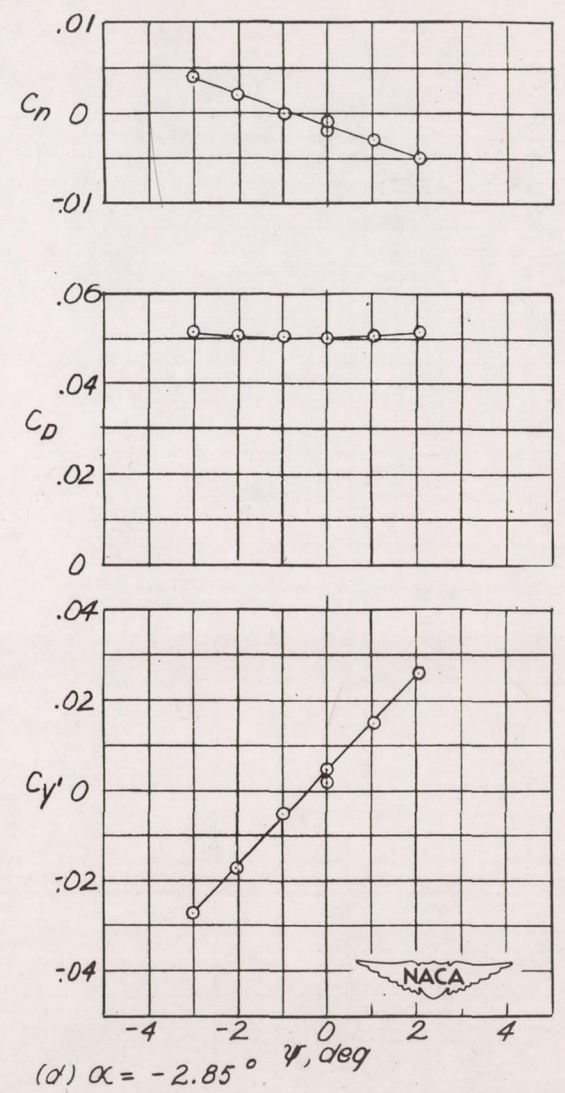
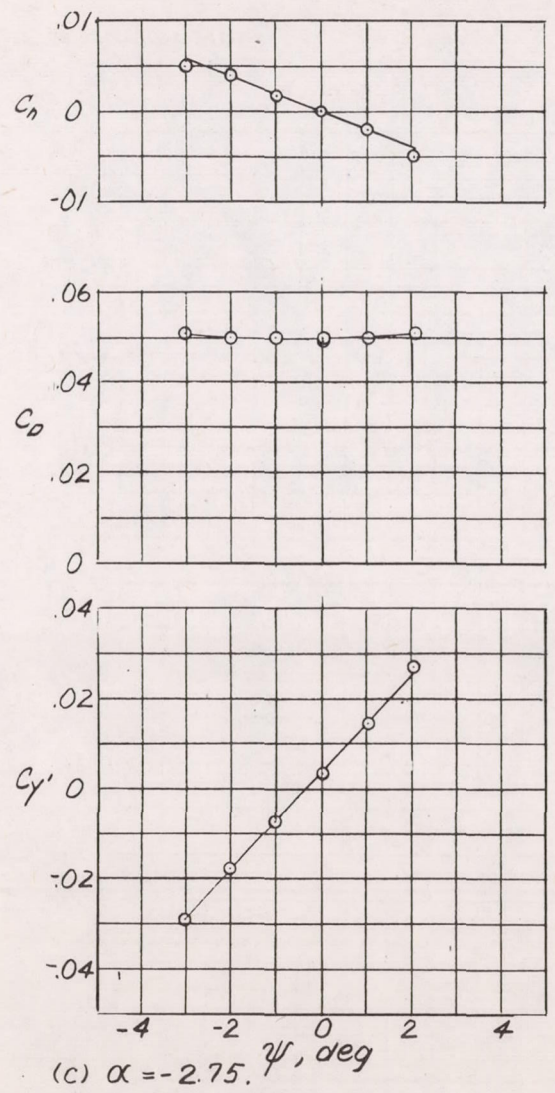


Figure 7 . - Concluded.

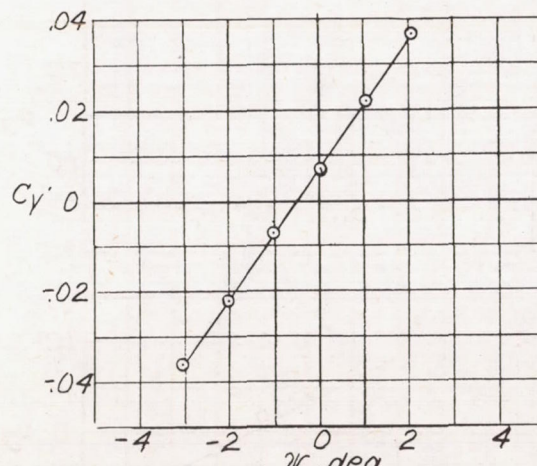
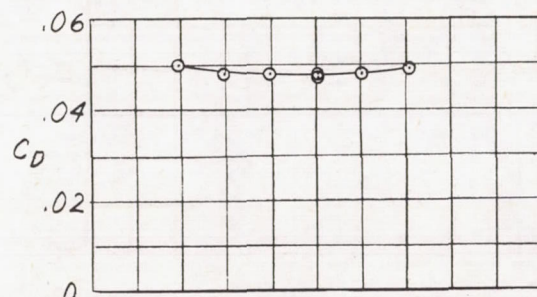
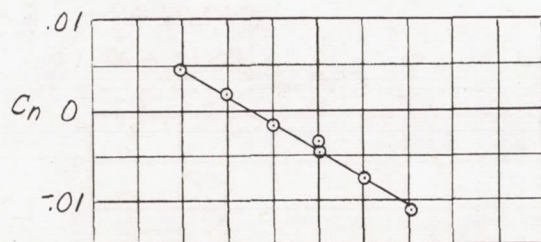
(a)  $\alpha = -1.47^\circ$ .

Figure 8 . - Variation of  $C_n$ ,  $C_{y'}$  and  $C_D$  with angle of yaw for Model 2;  $M=1.90$ .

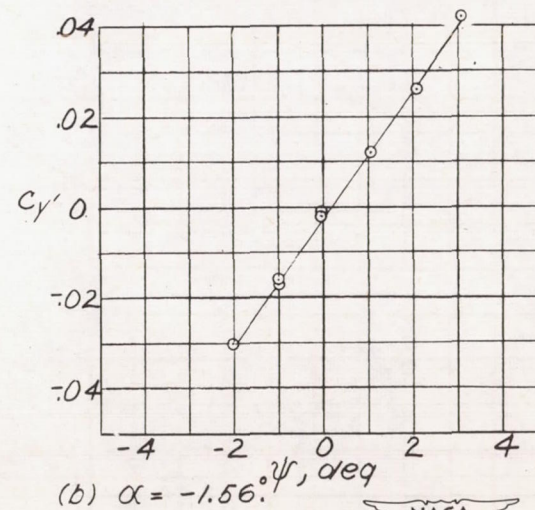
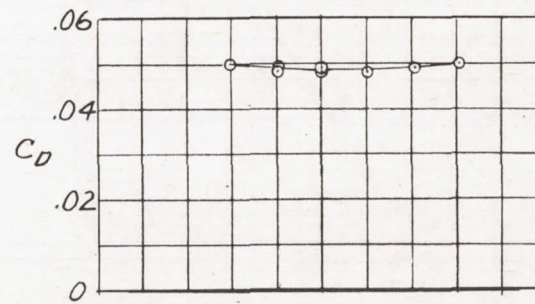
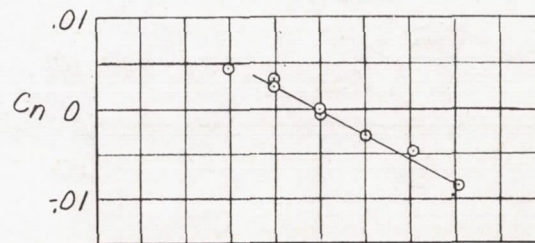
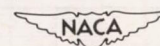
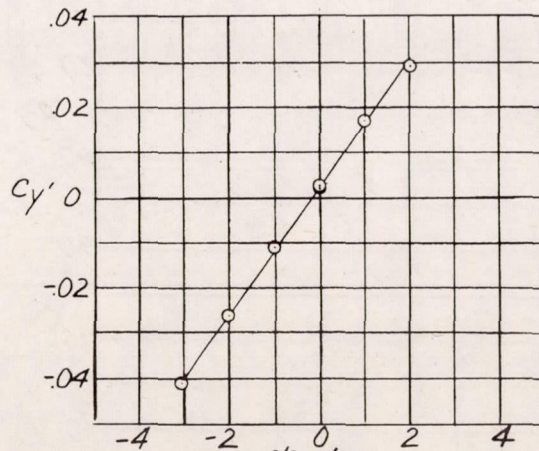
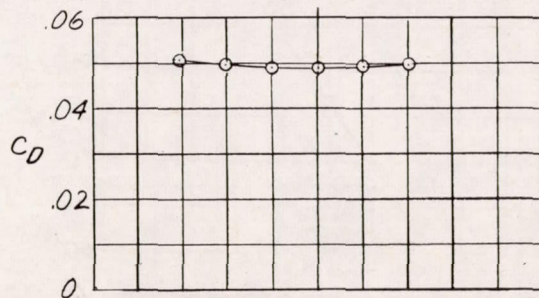
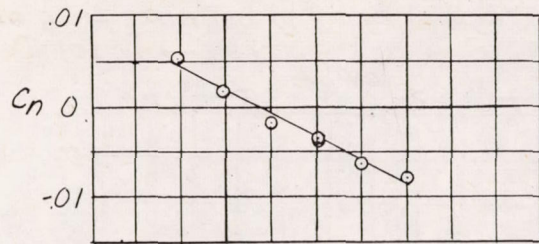
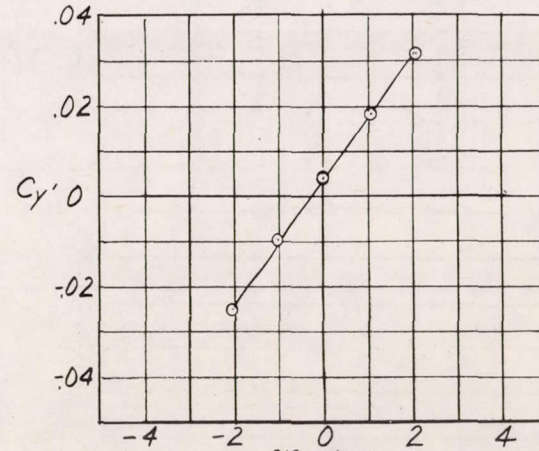
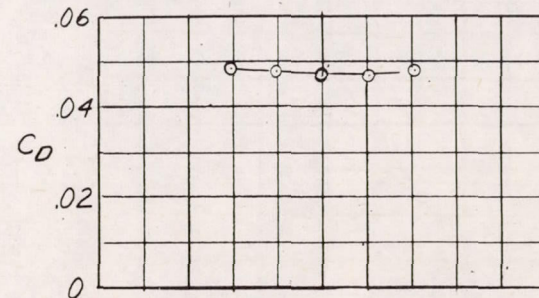
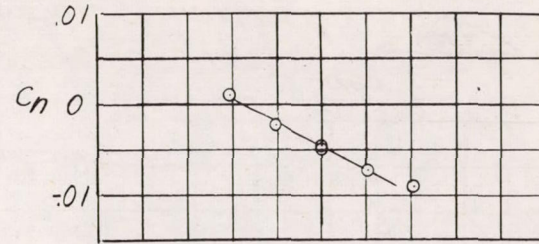
(b)  $\alpha = -1.56^\circ$ .

Figure 8 . - Continued.





(c)  $\alpha = -1.92^\circ$ ,  $\psi$ , deg



(d)  $\alpha = -2.23^\circ$ ,  $\psi$ , deg

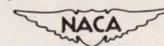


Figure 8. - Continued.

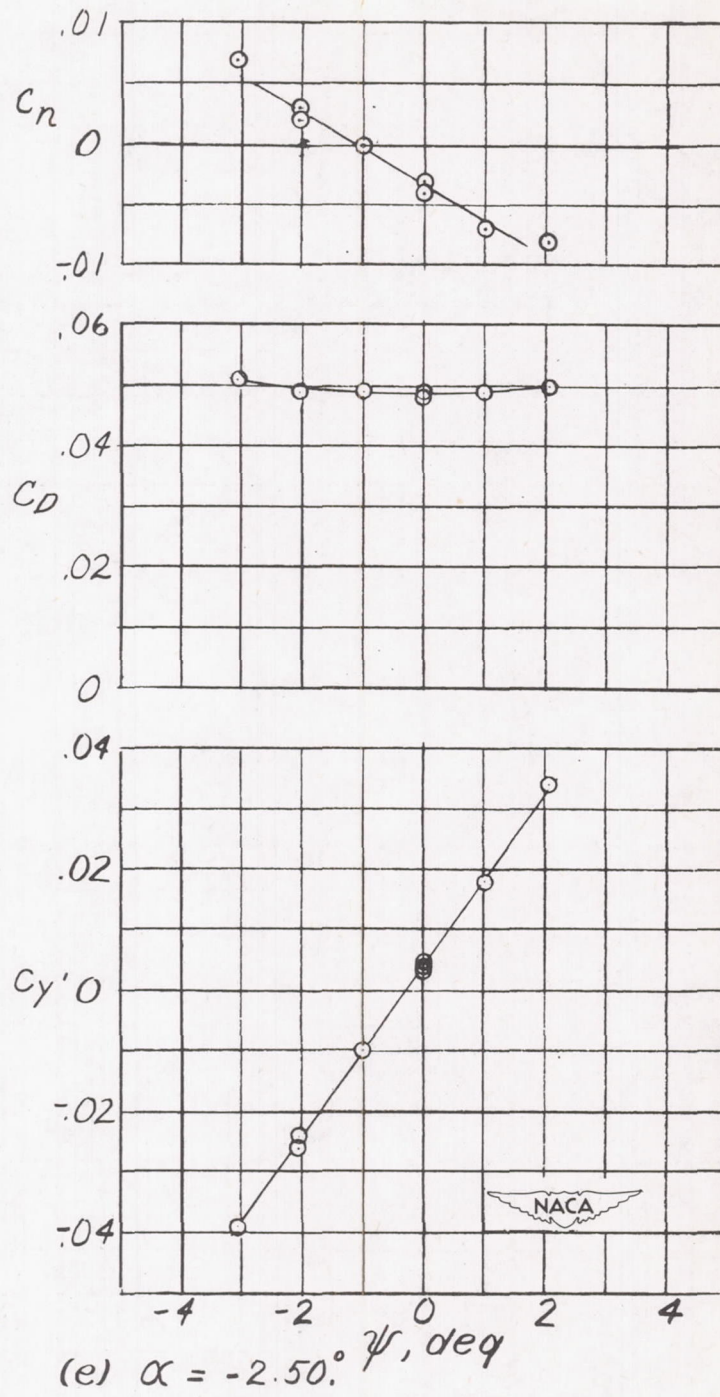


Figure 8 . - Concluded .

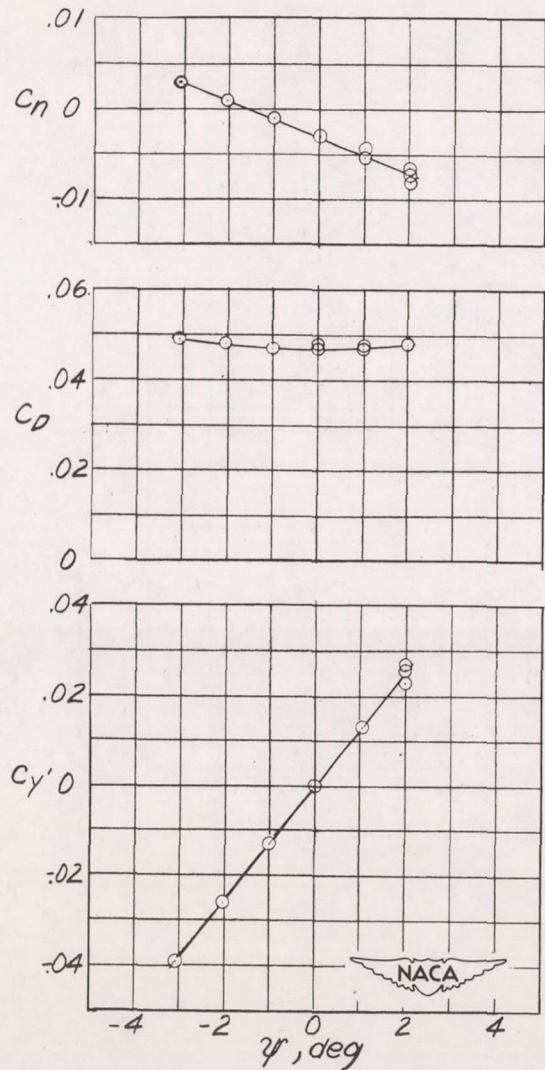


Figure 9. - Variation of  $C_n$ ,  $C_{y'}$  and  $C_D$  with angle of yaw for Model 2 with Ventral fin off;  $M = 1.90$ ;  $\alpha = -2.30$ .

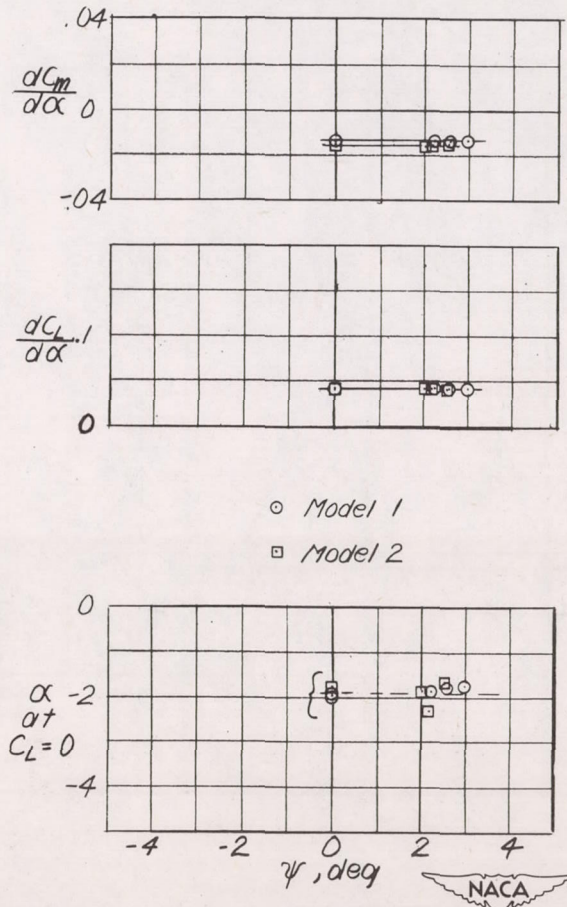


Figure 10. - Variation of  $dC_m/d\alpha$ ;  $dC_L/d\alpha$  and  $\alpha$  at  $C_L=0$  with angle of yaw for Models 1 and 2;  $M = 1.90$ .

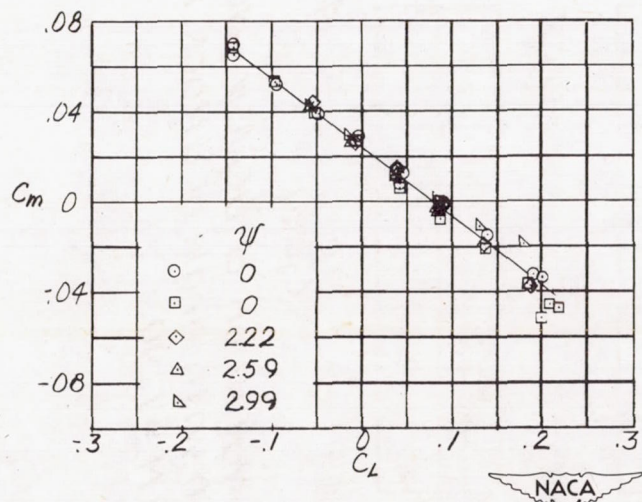


Figure 11. - Variation of  $C_m$  with  $C_L$  for angle of yaw for Model 1;  $M = 1.90$ .

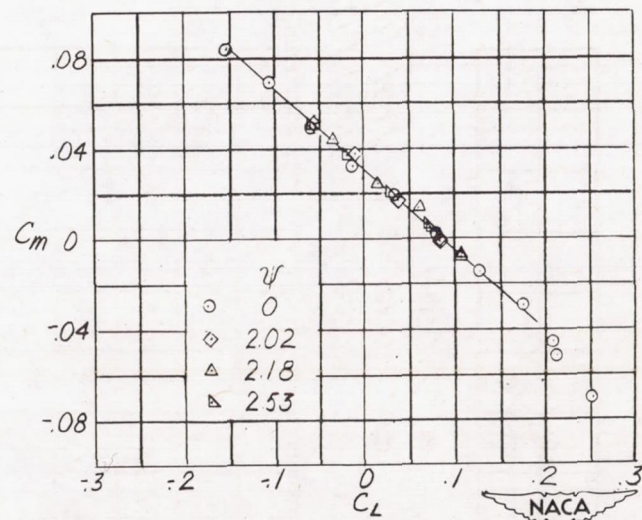


Figure 12. - Variation of  $C_m$  with  $C_L$  for angle of yaw for Model 2;  $M = 1.90$ .



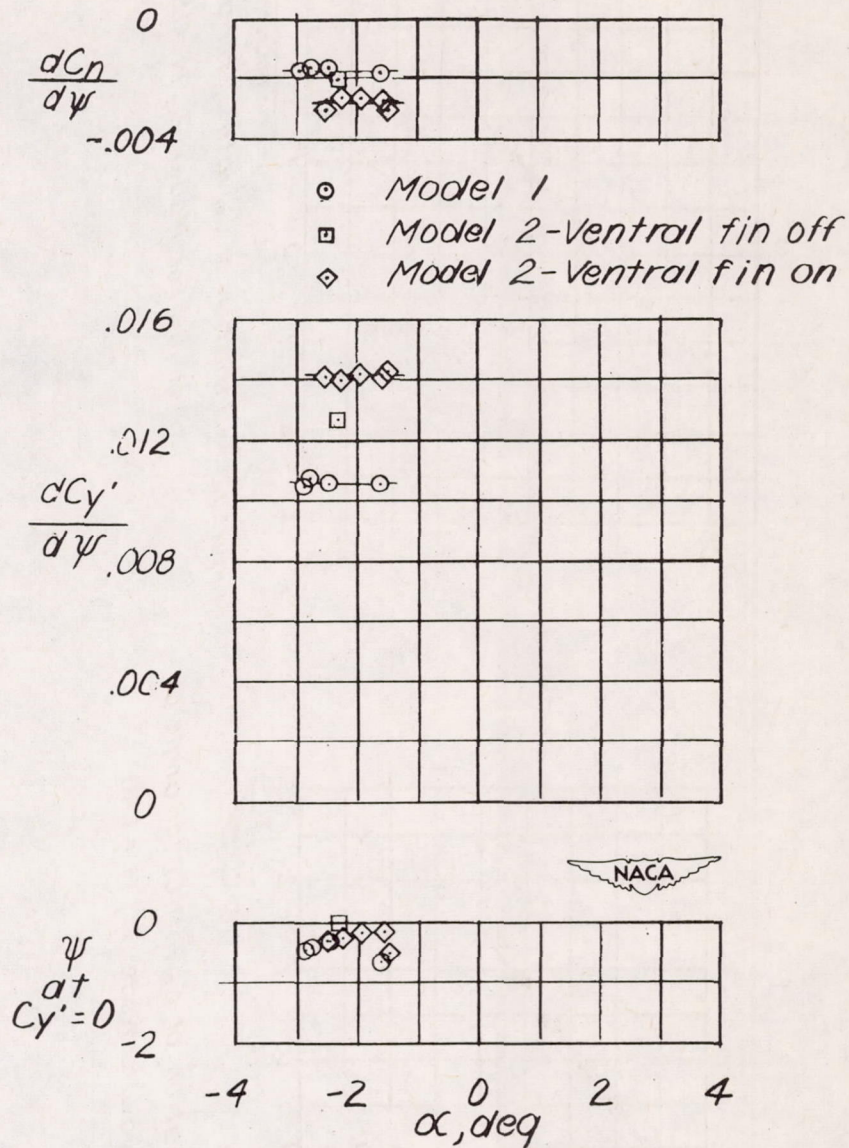


Figure 13. - Variation of  $dC_n/C_\psi$ ,  $dC_{\gamma'}/d\psi$  and  $\psi$  at  $C_{\gamma'}=0$  with angle of attack for Models 1 and 2;  $M=1.90$ .

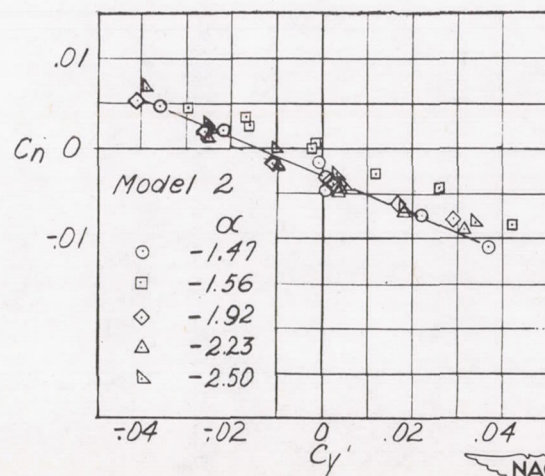
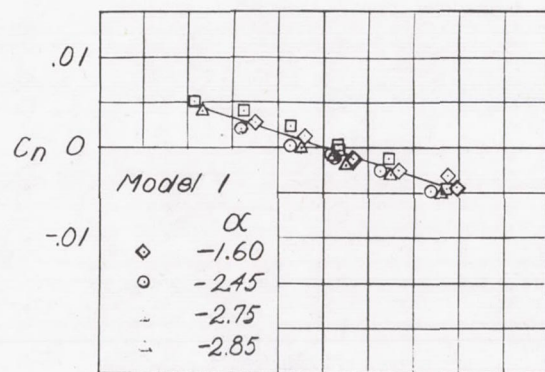


Figure 14. - Variation of  $C_n$  with  $C_{y'}$  for angles of attack for Models 1 and 2;  $M = 1.90$ .

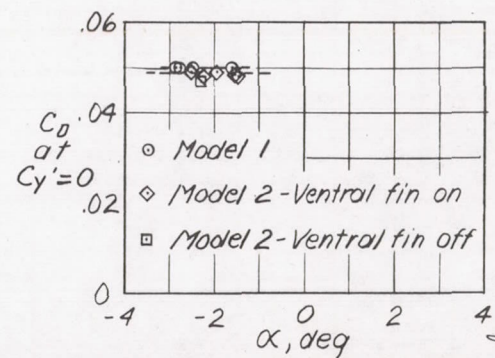
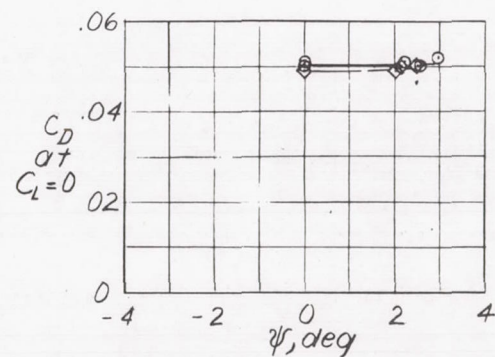


Figure 15. - Variation of  $C_D$  at  $C_L = 0$  and  $C_{y'} = 0$  with angles of attack and yaw for Models 1 and 2;  $M = 1.90$ .

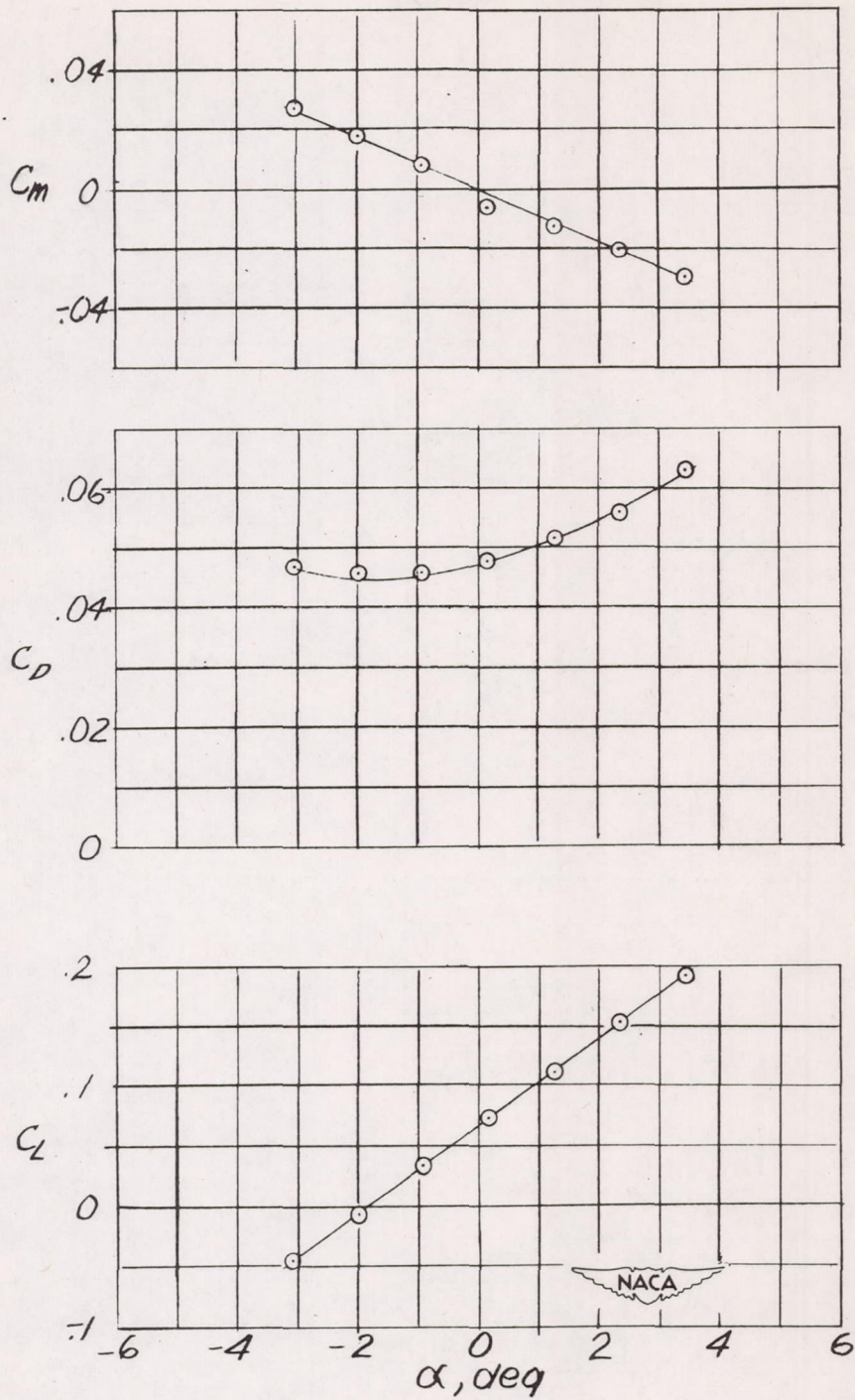


Figure 16. - Variation of  $C_m$ ,  $C_L$  and  $C_D$  with angle of attack for Model 1;  $M = 2.32$ ;  $\psi = 0$ .

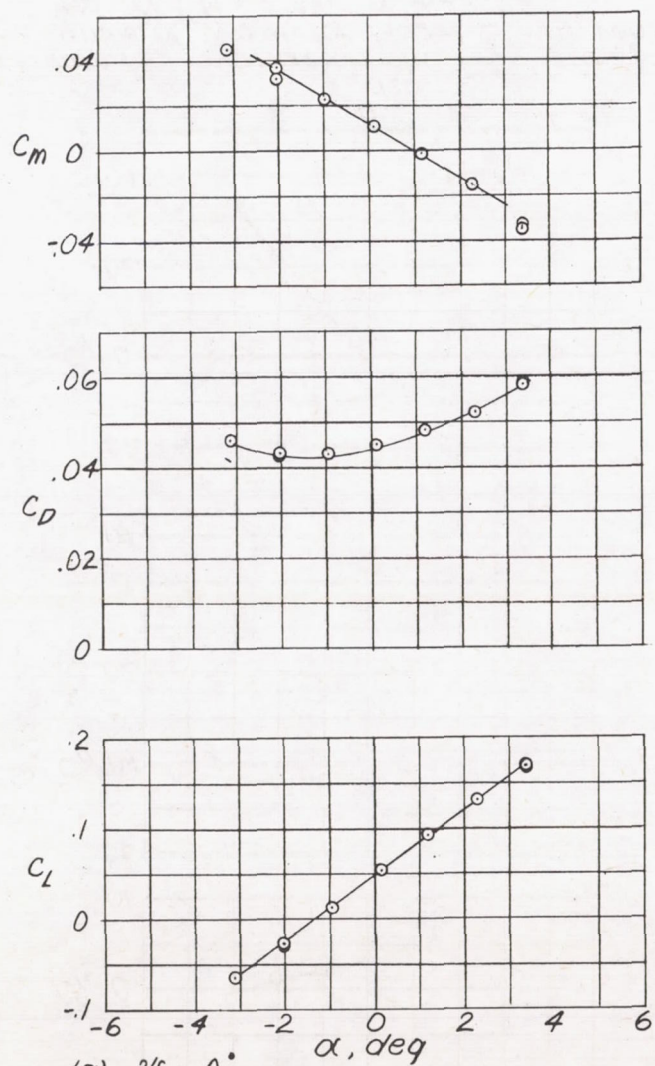


Figure 17. - Variation of  $C_m$ ,  $C_L$  and  $C_D$  with angle of attack for Model 2 with ventral fin off;  $M = 2.32$ .

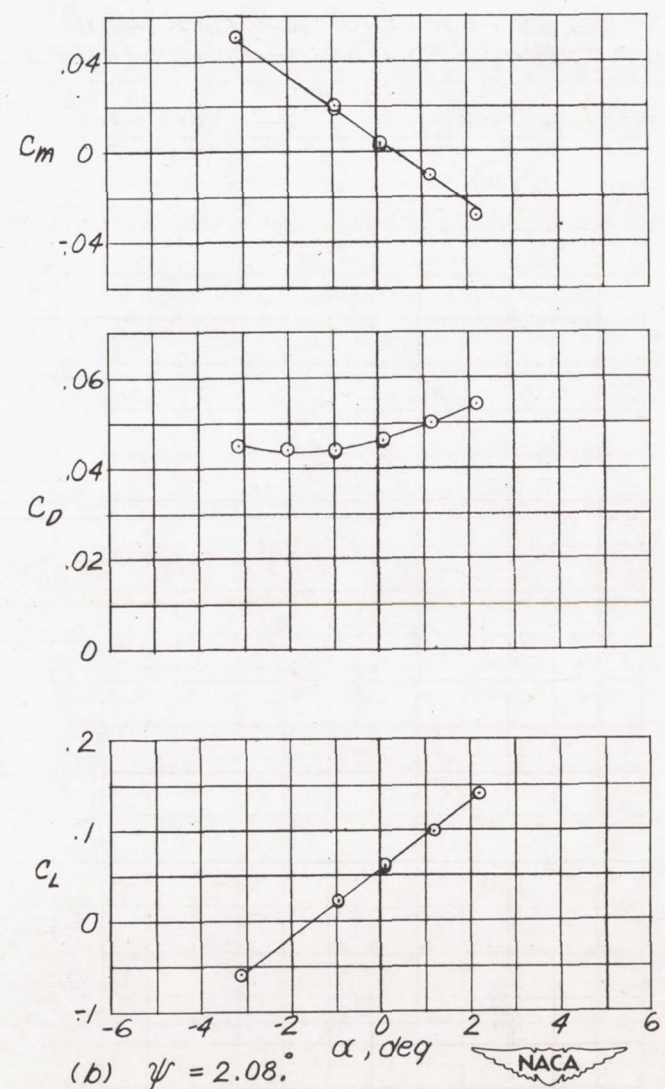
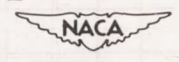


Figure 17. - Concluded.



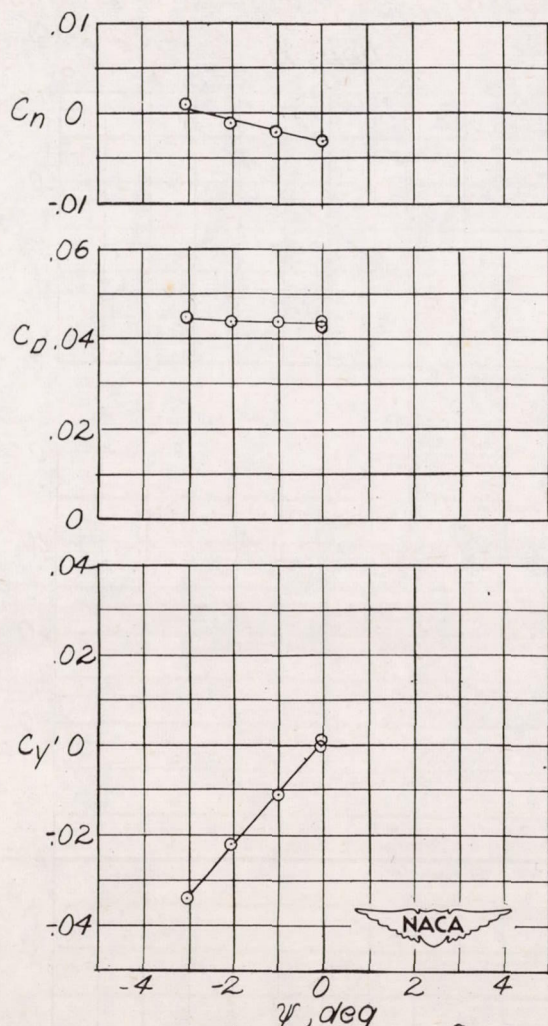


Figure 18. - Variation of  $C_n$ ,  $C_{y'}$  and  $C_D$  with angle of yaw for Model 2 with ventral fin off;  $M = 2.32$ ;  $\alpha = -2.22$ .

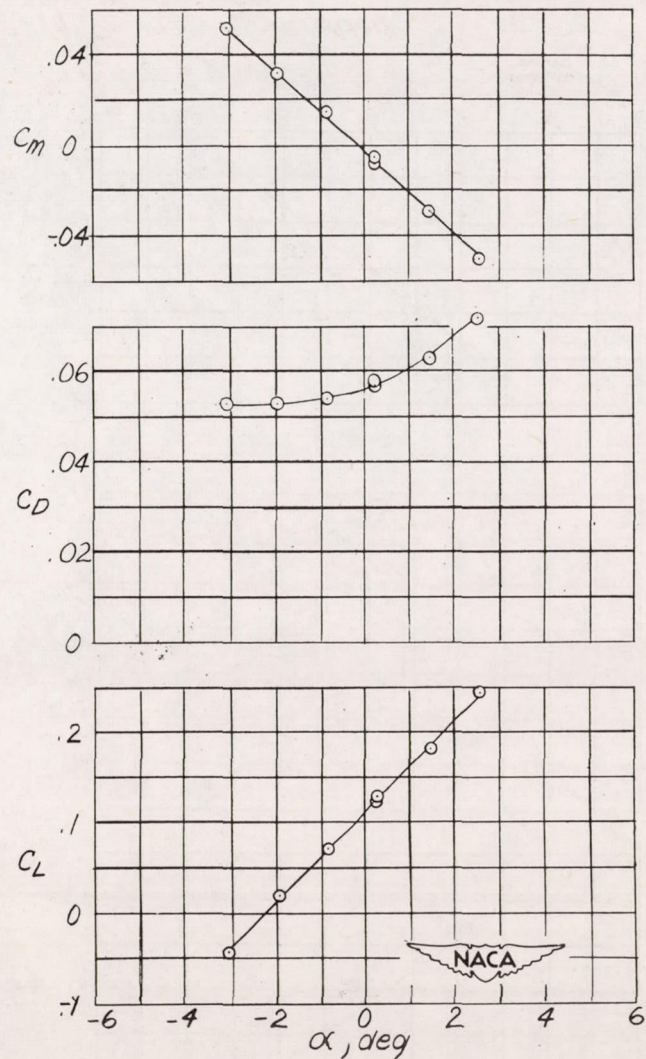
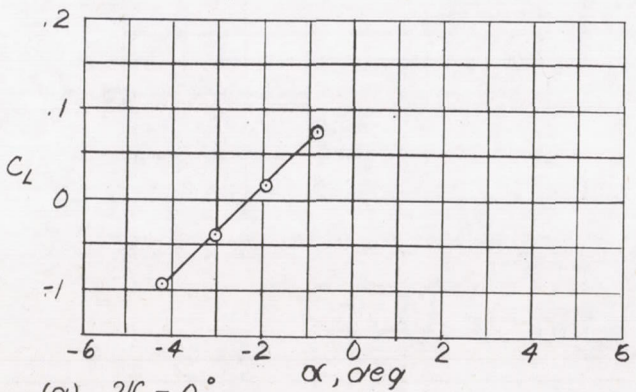
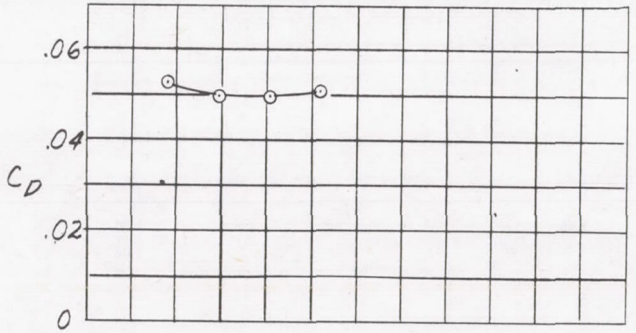
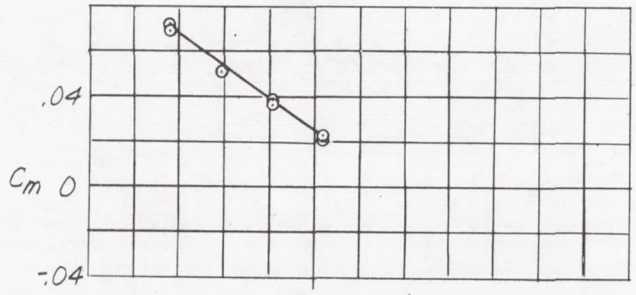
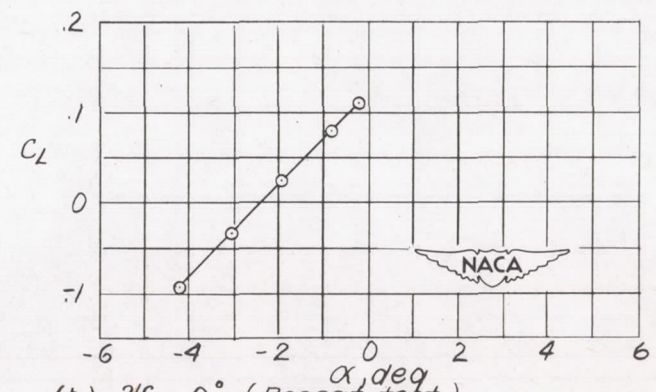
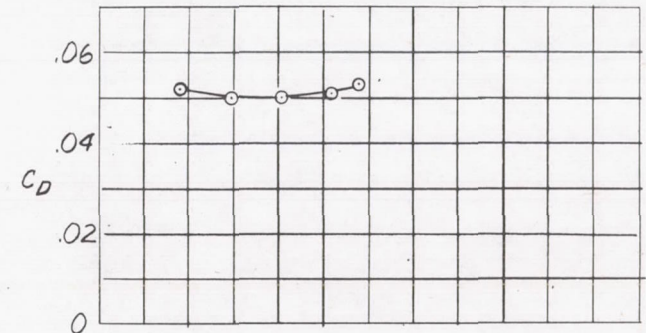
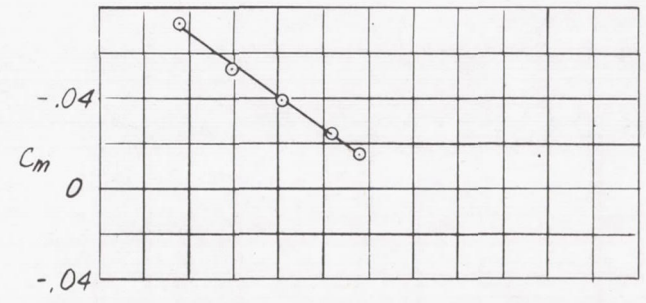


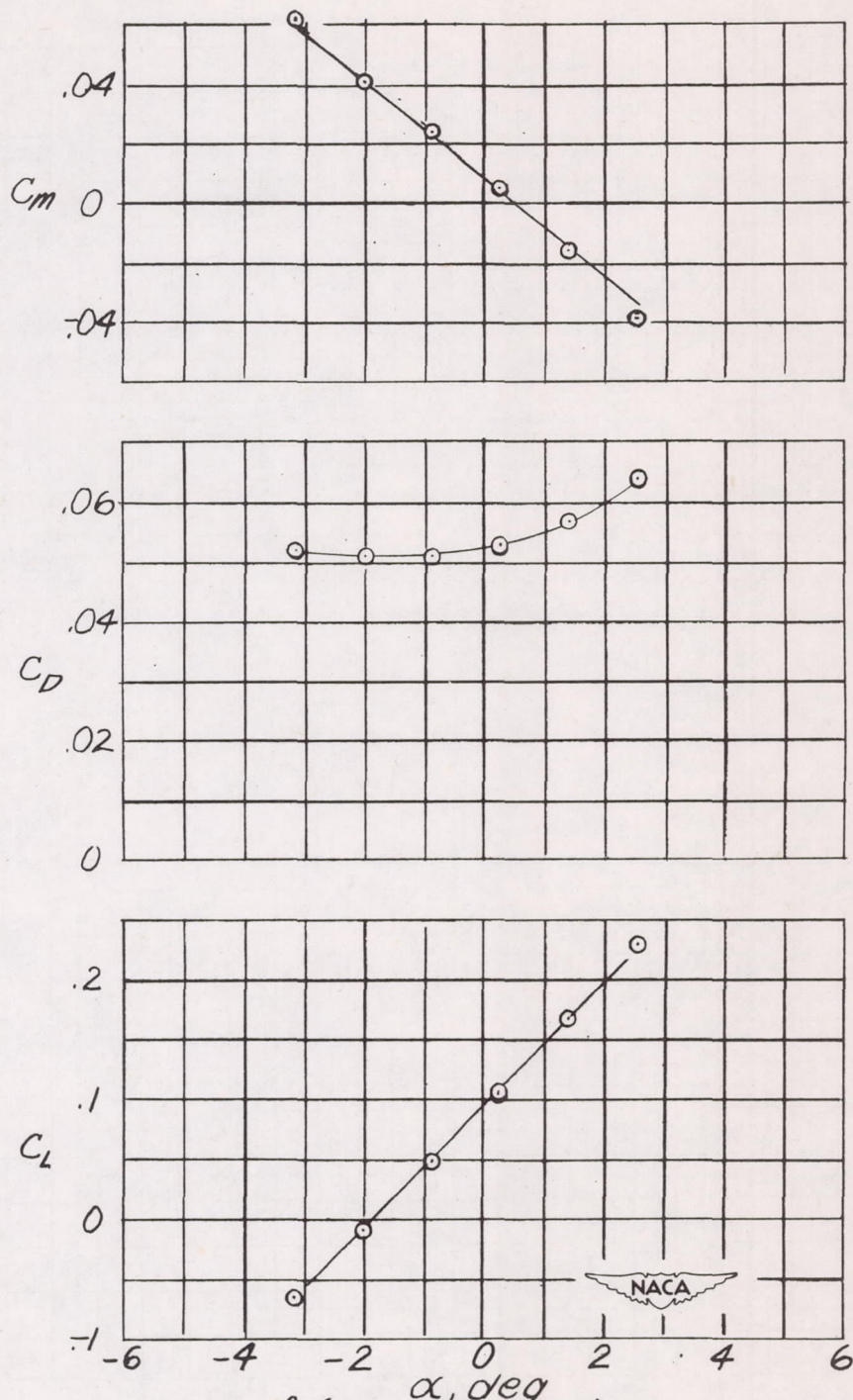
Figure 19. - Variation of  $C_m$ ,  $C_L$  and  $C_D$  with angle of attack for Model 1;  $M = 1.55$ ;  $\psi = 0^\circ$ .



(a)  $\psi = 0^\circ$   
 Figure 20. - Variation of  $C_m$ ,  $C_L$  and  $C_D$  with angle of attack for Model 2 with Ventral fin off;  $M = 1.55$ .

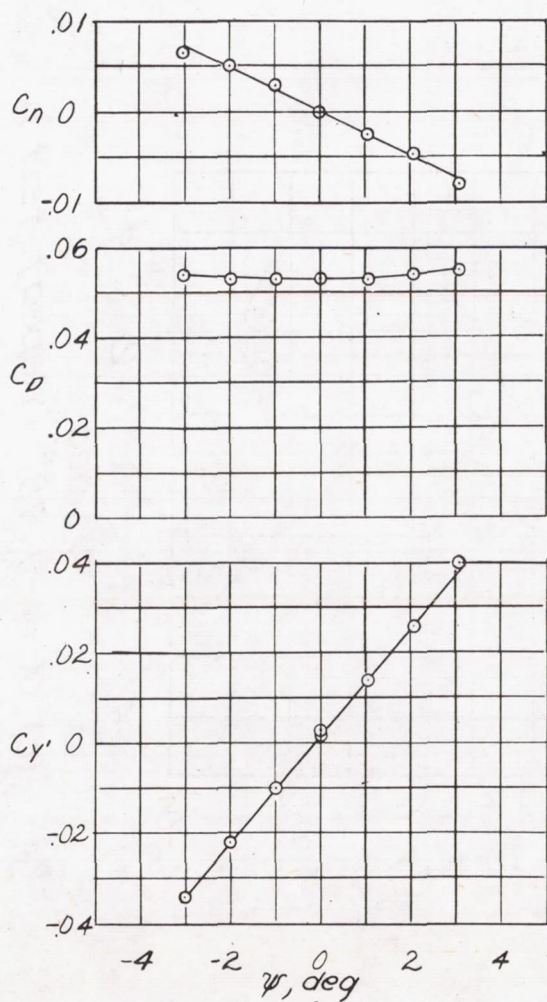


(b)  $\psi = 0^\circ$  (Repeat test).  
 Figure 20. - Continued.



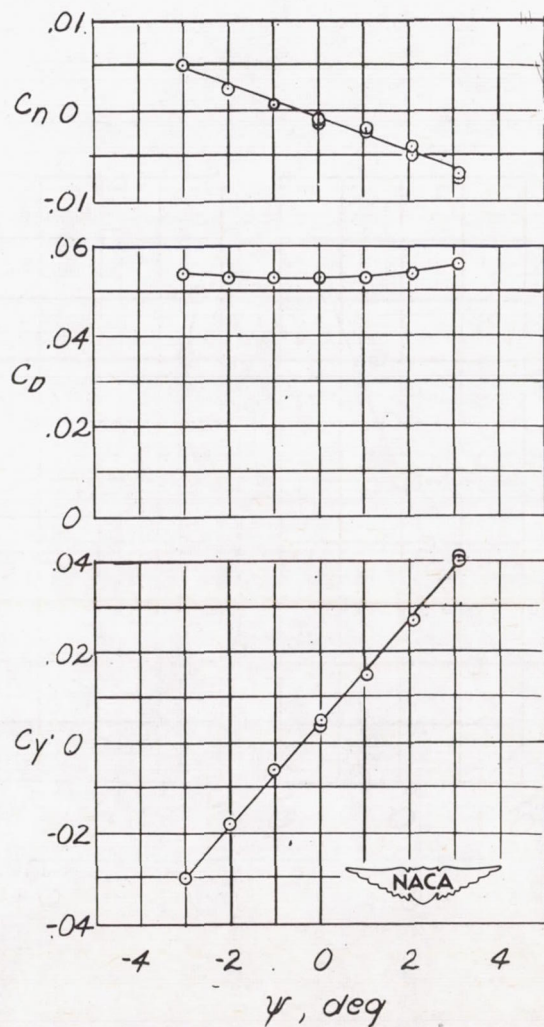
(c)  $\psi = 0^\circ$  (Repeat test).

Figure 20. - Concluded.



(a)  $\alpha = -1.78^\circ$

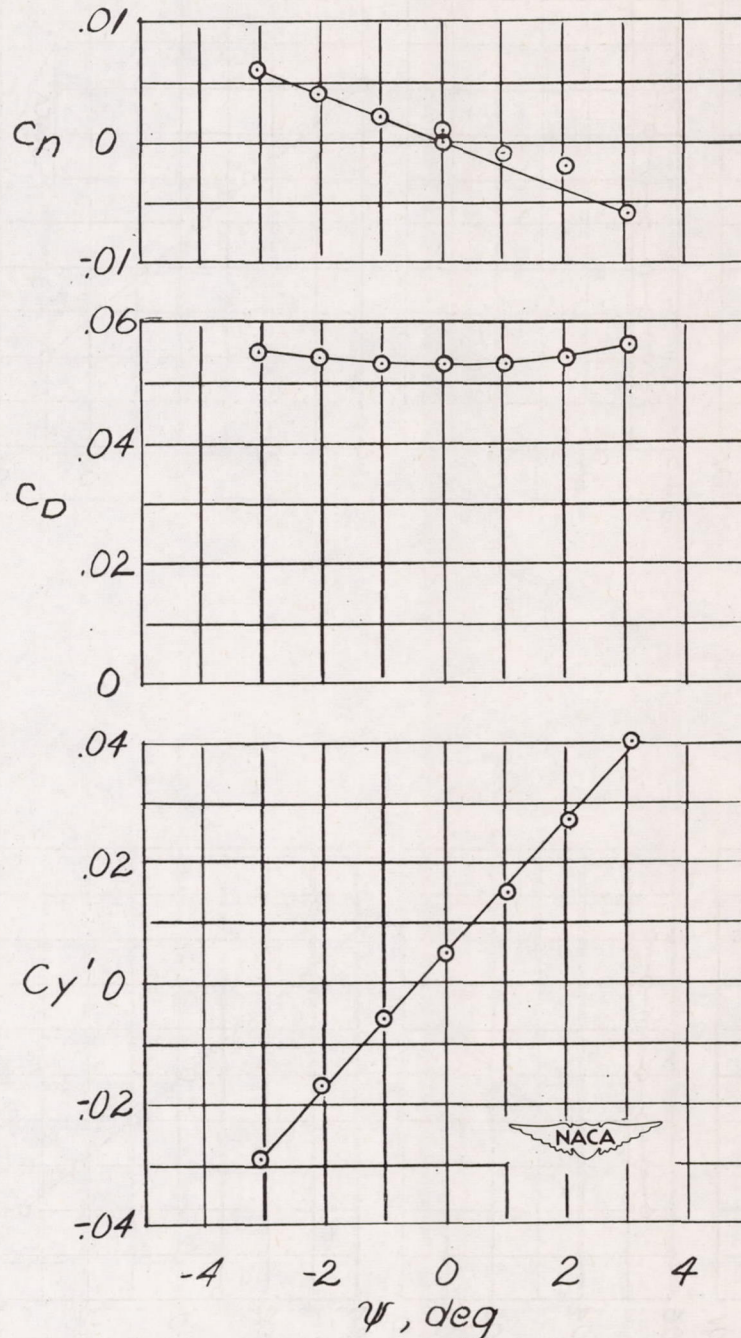
Figure 21. — Variation of  $C_n$ ,  $C_{y'}$  and  $C_D$  with angle of yaw for Model 1;  $M = 1.55$ .



(b)  $\alpha = -1.78^\circ$  (Repeat test).

Figure 21. — Continued.





(c)  $\alpha = -1.78^\circ$  (Repeat test).

Figure 21. - Concluded.

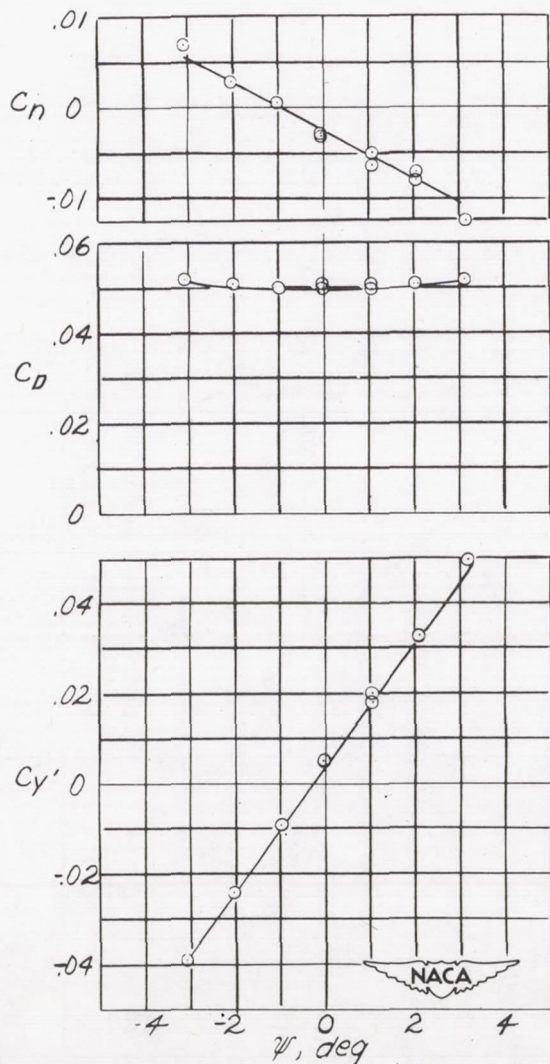


Figure 22 - Variation of  $C_n$ ,  $C_{y'}$  and  $C_D$  with angle of yaw for Model 2 with ventral fin off;  $M=1.55$ ;  $\alpha = -2.02$ .

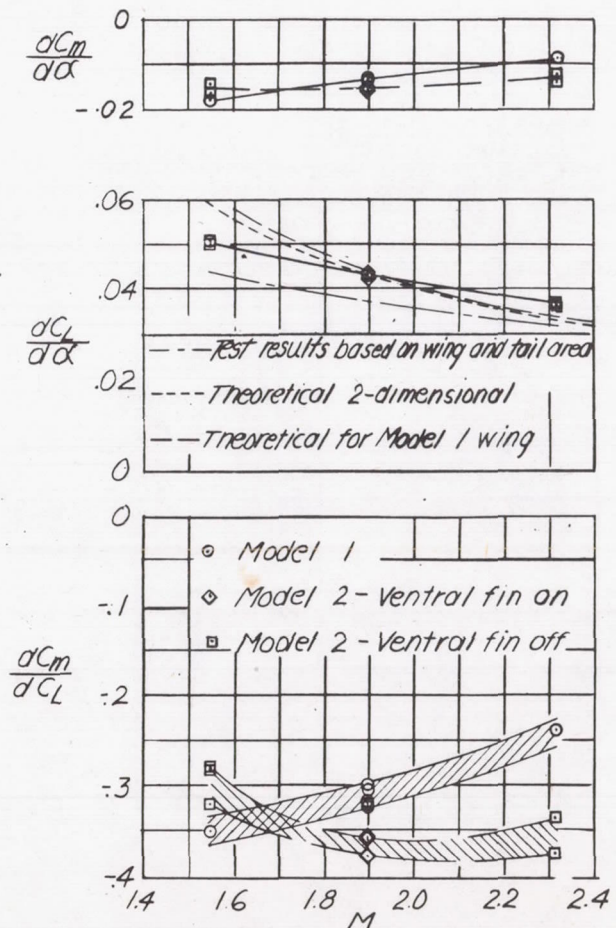


Figure 23. - Variation of  $\frac{dC_m}{d\alpha}$ ,  $\frac{dC_L}{d\alpha}$  and  $\frac{dC_m}{dC_L}$  with  $M$  for Models 1 and 2.

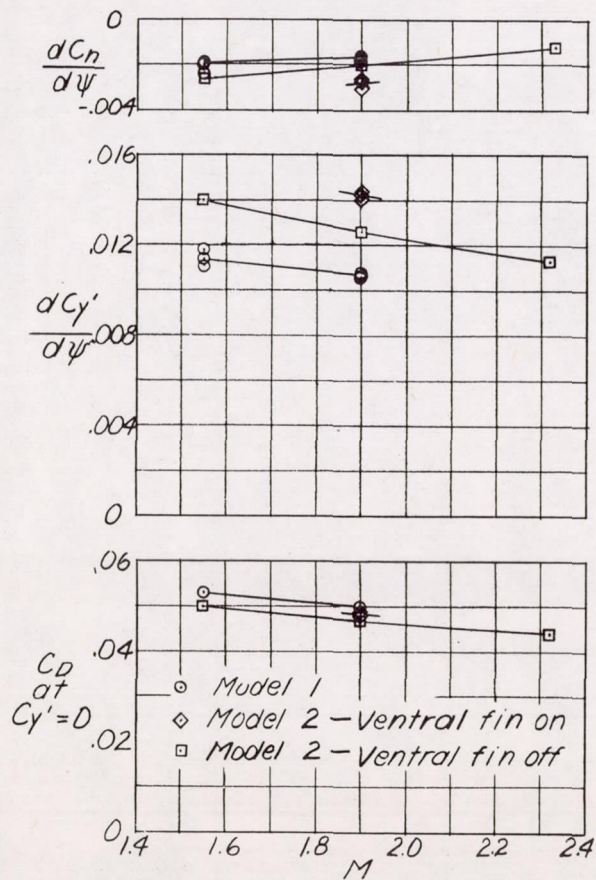


Figure 24. - Variation of  $\frac{dC_n}{d\psi}$ ,  $\frac{dC_{y'}}{d\psi}$  and  $C_D$  at  $C_{y'}=0$  with  $M$  for Models 1 and 2.

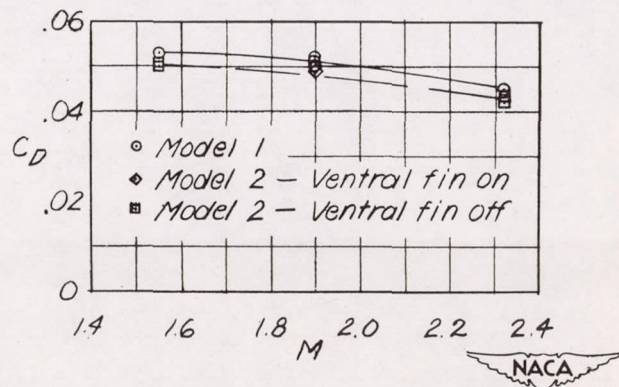
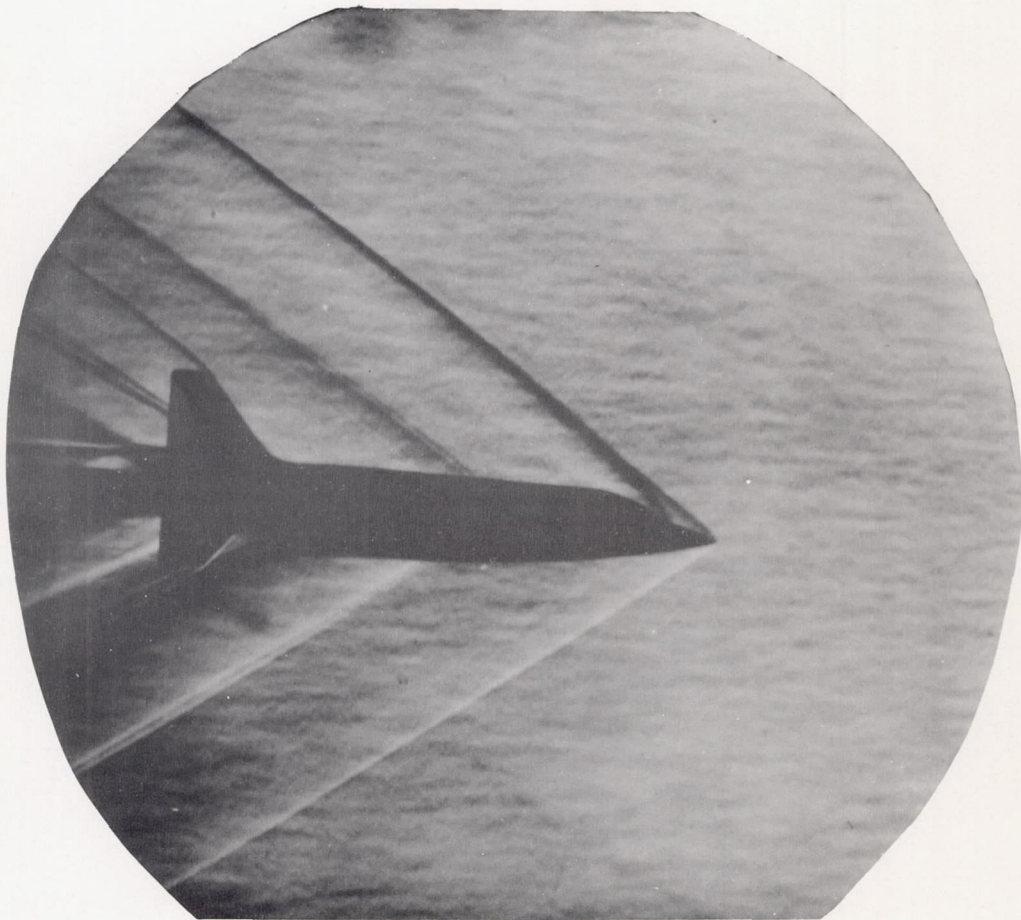


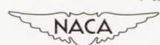
Figure 25. - Variation of  $C_D$  at  $C_L=0$  for Models 1 and 2.

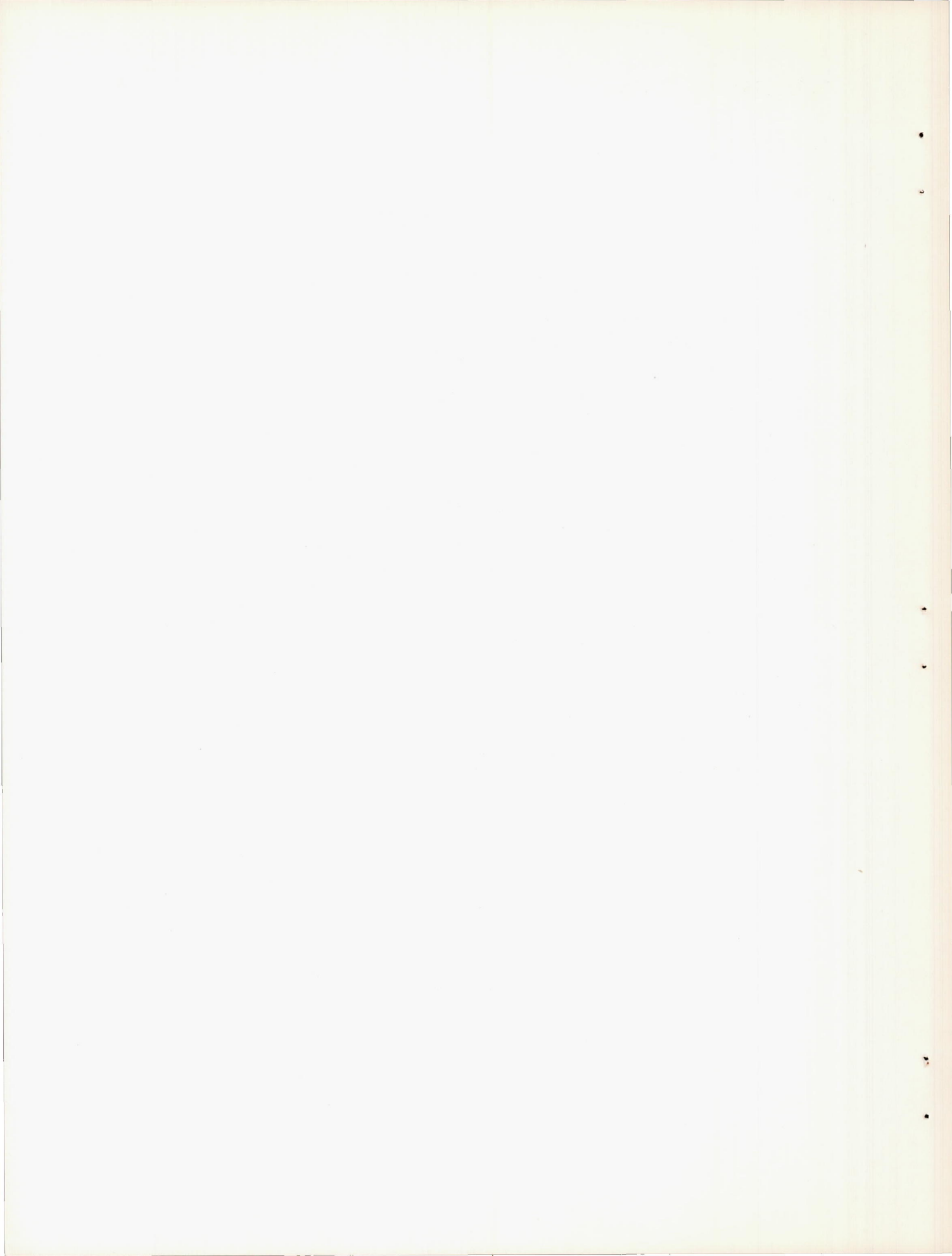


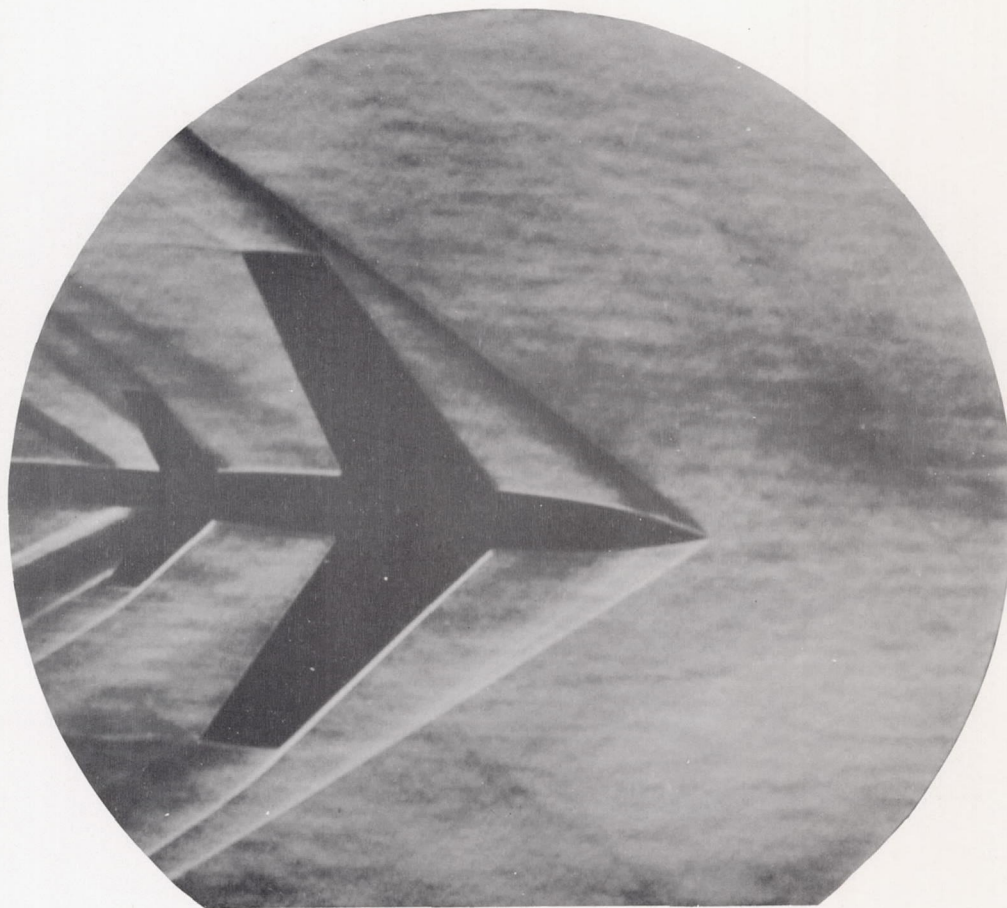


(a) Side view, model 1.

Figure 26.- Schlieren photograph with horizontal knife edges;  
M = 1.90.



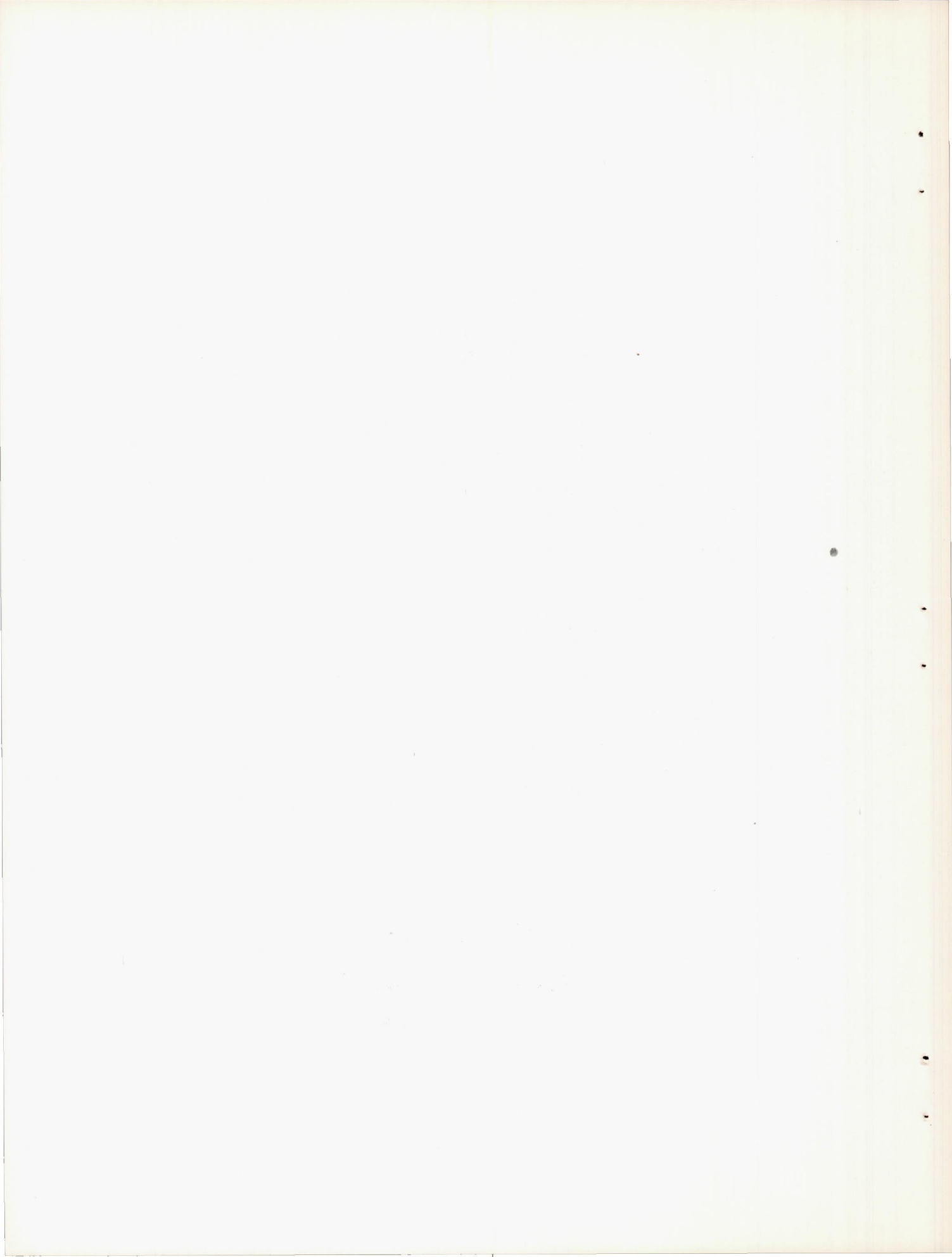




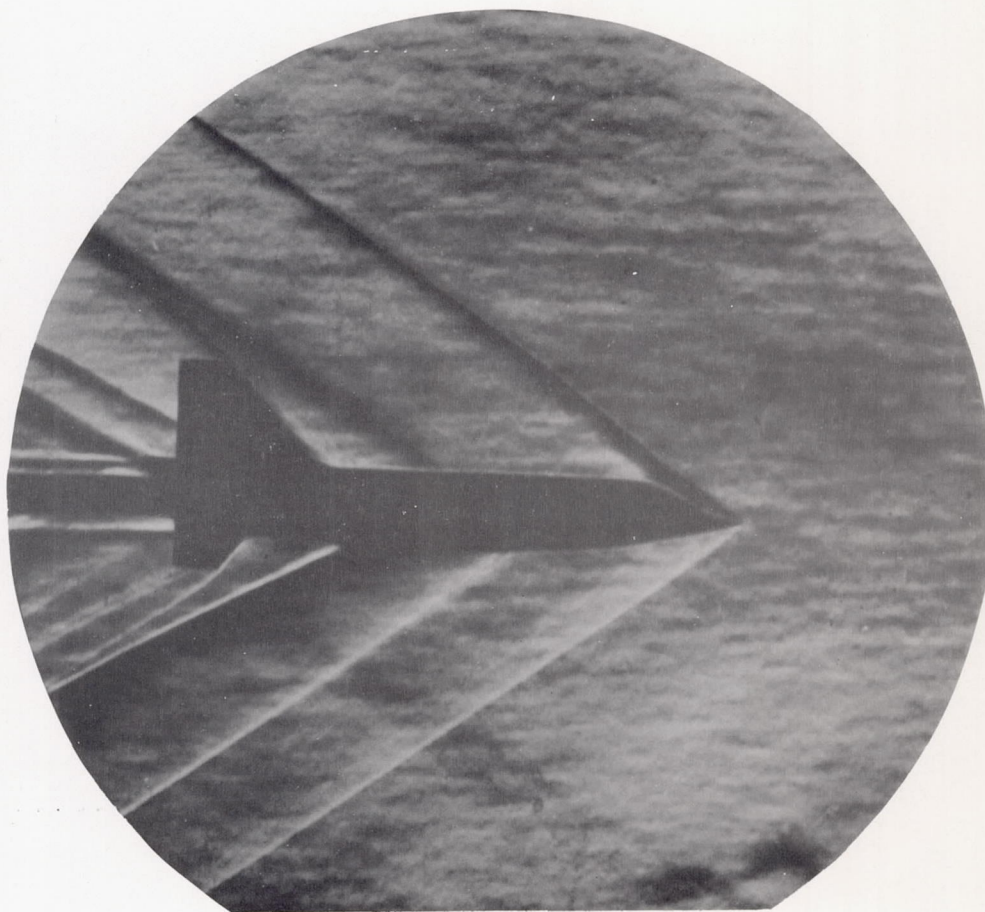
(b) Plan view, model 1.

Figure 26.- Continued.





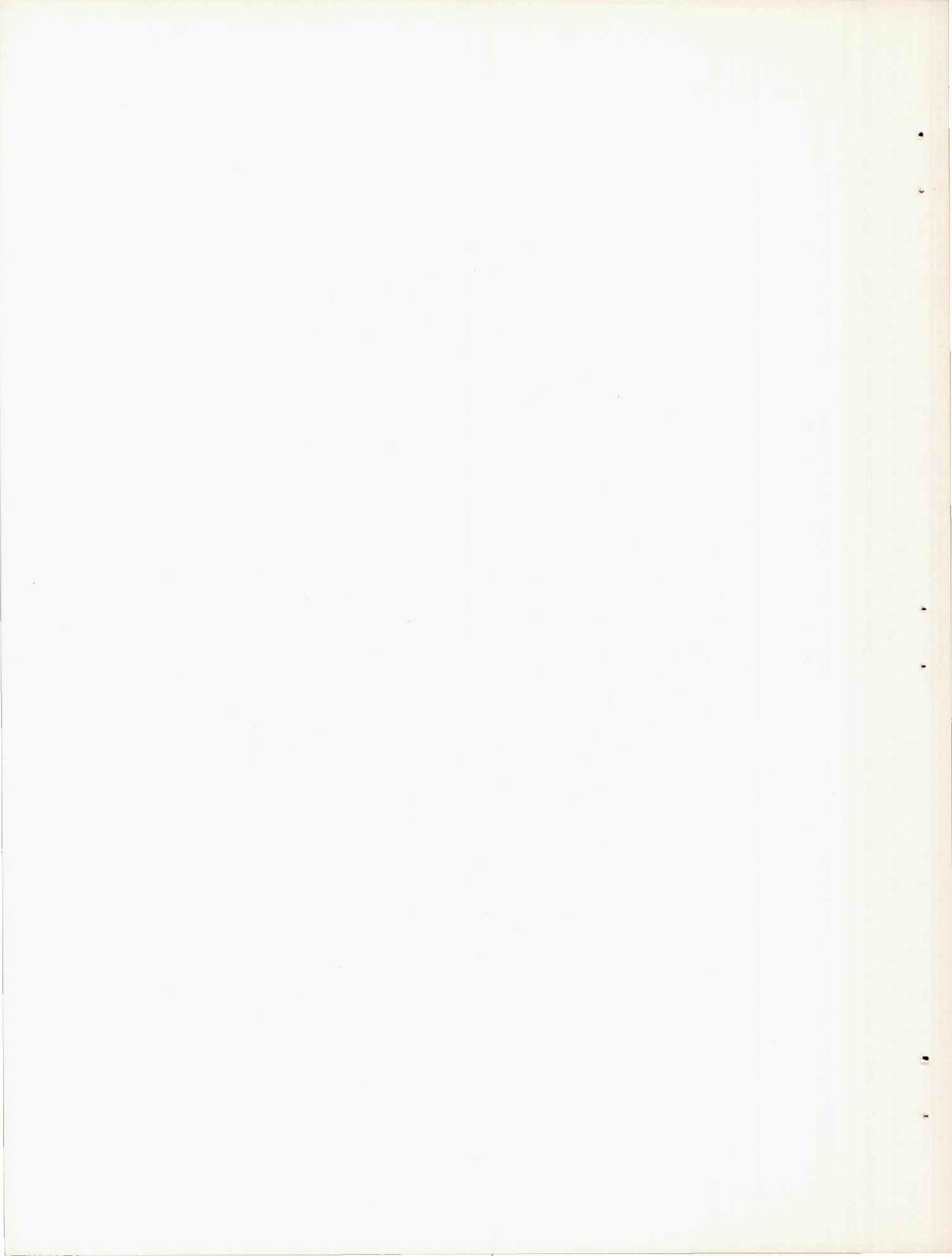




(c) Side view, model 2.

Figure 26.- Continued







(d) Plan view, model 2.

Figure 26.- Concluded.

